



OPEN ACCESS

EDITED BY
Yuan Lu,
Tsinghua University, China

REVIEWED BY
Karthik Raman,
Indian Institute of Technology Madras,
India
Jinyun Tang,
Berkeley Lab (DOE), United States
Mike Lyons,
Trinity College Dublin, Ireland

*CORRESPONDENCE
Rahul Sarpeshkar,
rahul.sarpeshkar@dartmouth.edu

SPECIALTY SECTION
This article was submitted to Synthetic
Biology,
a section of the journal
Frontiers in Bioengineering and
Biotechnology

RECEIVED 18 May 2022
ACCEPTED 09 August 2022
PUBLISHED 28 September 2022

CITATION
Deng Y, Beahm DR, Ran X, Riley TG and
Sarpeshkar R (2022), Rapid modeling of
experimental molecular kinetics with
simple electronic circuits instead of with
complex differential equations.
Front. Bioeng. Biotechnol. 10:947508.
doi: 10.3389/fbioe.2022.947508

COPYRIGHT
© 2022 Deng, Beahm, Ran, Riley and
Sarpeshkar. This is an open-access
article distributed under the terms of the
[Creative Commons Attribution License
\(CC BY\)](https://creativecommons.org/licenses/by/4.0/). The use, distribution or
reproduction in other forums is
permitted, provided the original
author(s) and the copyright owner(s) are
credited and that the original
publication in this journal is cited, in
accordance with accepted academic
practice. No use, distribution or
reproduction is permitted which does
not comply with these terms.

Rapid modeling of experimental molecular kinetics with simple electronic circuits instead of with complex differential equations

Yijie Deng¹, Douglas Raymond Beahm¹, Xinping Ran¹,
Tanner G. Riley² and Rahul Sarpeshkar^{1,3*}

¹Thayer School of Engineering, Dartmouth College, Hanover, NH, United States, ²School of Undergraduate Arts and Sciences, Dartmouth College, Hanover, NH, United States, ³Departments of Engineering, Microbiology and Immunology, Physics, and Molecular and Systems Biology, Dartmouth College, Hanover, NH, United States

Kinetic modeling has relied on using a tedious number of mathematical equations to describe molecular kinetics in interacting reactions. The long list of differential equations with associated abstract variables and parameters inevitably hinders readers' easy understanding of the models. However, the mathematical equations describing the kinetics of biochemical reactions can be exactly mapped to the dynamics of voltages and currents in simple electronic circuits wherein voltages represent molecular concentrations and currents represent molecular fluxes. For example, we theoretically derive and experimentally verify accurate circuit models for Michaelis-Menten kinetics. Then, we show that such circuit models can be scaled via simple wiring among circuit motifs to represent more and arbitrarily complex reactions. Hence, we can directly map reaction networks to equivalent circuit schematics in a rapid, quantitatively accurate, and intuitive fashion without needing mathematical equations. We verify experimentally that these circuit models are quantitatively accurate. Examples include 1) different mechanisms of competitive, noncompetitive, uncompetitive, and mixed enzyme inhibition, important for understanding pharmacokinetics; 2) product-feedback inhibition, common in biochemistry; 3) reversible reactions; 4) multi-substrate enzymatic reactions, both important in many metabolic pathways; and 5) translation and transcription dynamics in a cell-free system, which brings insight into the functioning of all gene-protein networks. We envision that circuit modeling and simulation could become a powerful scientific communication language and tool for quantitative studies of kinetics in biology and related fields.

KEYWORDS

biological circuits, cell-free system, kinetic modeling, michaelis-menten equation, biochemical engineering, circuit modeling, enzyme kinetics, reversible reactions

1 Introduction

Kinetic modeling has been a powerful tool for studying biological systems from simple enzymatic reactions to metabolic pathways, drug kinetics in hosts, gene circuits in synthetic biology, and host-pathogen interactions (Alves et al., 2006; Resat et al., 2009; Bevc et al., 2011; Eshtewy and Scholz, 2020; Néant et al., 2021). Modeling molecular kinetics can provide quantitative insights and mechanistic understandings of biological systems. However, kinetic modeling of biological processes relies on a substantial number of mathematical equations to describe even simple biochemical reactions. The heavy dependence on long and tedious differential equations hinders many biologists from appreciating and taking advantage of kinetic modeling as a powerful tool for studying biological questions. In particular, for many biological researchers, the long list of parameters and abstract terms that are used during the process of mathematical derivation are exhausting and difficult to follow. In addition, it can be challenging to resolve complex, nonlinear, coupled differential equations that require sophisticated algorithms/programs including numerical approaches (Bevc et al., 2011) for simulating time-course kinetics.

However, ordinary differential equations (ODEs), commonly used to model biochemical reactions and processes, can be represented by simple electronic circuits (Sarpeshkar, 2010; Teo and Sarpeshkar, 2020) in a mathematically exact fashion. We can thus take advantage of electronic design software to design circuits *in silico* that represent the kinetics of the target system and then run simulations in software without the need to manufacture the physical circuits (Teo et al., 2019a; Teo and Sarpeshkar, 2020). Therefore, not only can we visualize all the math equations in one circuit but also solve them by just running simulations on the circuit. Using virtual electronic circuits enables one to do rapid kinetic modeling of biochemical reactions without deriving tedious differential equations. In addition, circuit simulation in electronic design software is able to provide accurate time-course dynamics, not just equilibrium solutions. Circuit software has built-in algorithms to automatically solve underlying equations represented by the circuits, which has evolved over 75 + years of circuit design for multiple forms of design and analysis (Sarpeshkar, 2010).

The overall mechanism of the simulation is that, given some preset parameters of a circuit, the voltage and current at any node of the circuit at any time are readily available upon simulation; these voltages and currents exactly represent the corresponding molecular concentrations and molecular reaction flux rates, respectively. For example, we have used electronic circuits to model and simulate complex biological processes including genetic circuits in synthetic biology (Daniel et al., 2013; Teo et al., 2015; Zeng et al., 2018); kinetics of microbial growth and energetics (Deng et al., 2021); tissue homeostasis (Teo et al., 2019b); and virus-host interactions (Beahm et al., 2021).

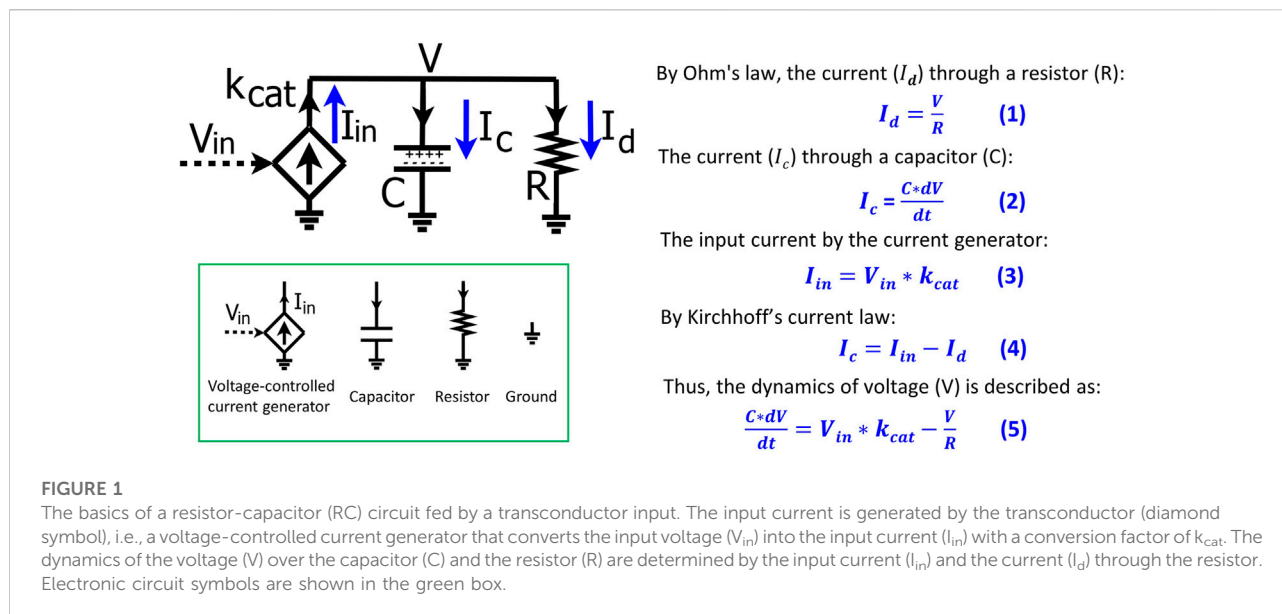
However, there are gaps in biologists' understanding of electronic circuits and the underlying mathematics; and, in their understanding of the analogy of circuit variables to reaction kinetic parameters. These gaps have prevented many researchers from understanding circuit models and using circuits to do kinetic modeling in practice.

Therefore, an important goal of this work is to illustrate how the mathematics describing the kinetics of biochemical reactions can be exactly mapped to electronic circuits; and, to demonstrate how to use such circuits to do rapid kinetic modeling without deriving math equations. To demonstrate the circuit modeling approach, we start with the basics of a simple resistor-capacitor (RC) circuit and its use in representing the dynamics of a simple biochemical reaction. We then illustrate how to use circuits to model an enzyme-substrate reaction that is characterized by Michaelis-Menten kinetics, one of the most fundamental processes in biology. Next, we develop widely applicable circuit motifs for biochemical reactions including different types of enzyme inhibition, multi-molecular binding, multi-substrate reactions, reversible reactions, and DNA transcription and translation. Notably, these circuit models are validated by good fits to our experimental data. These fundamental circuit motifs can be easily used to construct large-scale circuit models for complicated biological networks/pathways without using cumbersome math equations; mature circuit-simulation software can then automatically provide accurate solutions including the time-course kinetics of molecules. Large circuit models are useful in analyzing the behavior of biological systems and to discover natural algorithms and architectures in biology. In addition, our approach provides mechanistic insights into fundamental biochemical reactions, such as the kinetics of enzyme inhibition and the kinetics of sequential binding reactions.

2 Results

2.1 Mapping a basic chemical reaction to a simple electronic circuit

To help biologists understand the basic mathematics of electronic circuits, we first derive, step-by-step, the basics of a simple RC circuit that is foundational for kinetic modeling in biological systems. The RC circuit consists of a resistor (R), a capacitor (C), and an input current (I_{in}) that is generated by a voltage-controlled current generator (a 'transconductor') that converts the input voltage (V_{in}) into the current (I_{in}) (Figure 1). In electronics, a current is denoted by I (measured in Amps, A), a voltage is denoted by V (measured in Volts, V), a resistor has a resistance of R (measured in Ohms, Ω), and a capacitor has a capacitance of C (measured in Farad, $F = A \cdot s/V$). As shown in Figure 1, the input current (I_{in}) goes through the capacitor and the resistor; the voltage (V) on the capacitor and



the resistor keeps increasing until it reaches a steady state wherein the capacitor is fully charged; thereafter, all the input current (I_{in}) goes through the resistor. To describe how the voltage (V) changes over time, we first calculate three currents in the circuit as below:

According to Ohm's law, the current (I_d) going through the resistor is defined by Eq. 1:

$$I_d = \frac{V}{R} \quad (1)$$

The total charge on the capacitor is Q and thus the current (I_c) through the capacitor is described as:

$$I_c = \frac{dQ}{dt} = \frac{C \cdot dV}{dt} \quad (2)$$

As mentioned above, the input current (I_{in}) is generated by a voltage-controlled current source (the diamond-shaped device or 'transconductor' in Figure 1) that converts the input voltage (V_{in}) into the current with a conversion factor (k_{cat}), and thus we have:

$$I_{in} = V_{in} * k_{cat} \quad (3)$$

The input current is split into I_c and I_d in the circuit. By Kirchoff's current law, we have:

$$I_c = I_{in} - I_d \quad (4)$$

We substitute Eqs 1–3 into Eq. 4 and thus have Eq. 5 that describes the voltage dynamics in the RC circuit:

$$\frac{C \cdot dV}{dt} = I_{in} - I_d = V_{in} * k_{cat} - \frac{V}{R} \quad (5)$$

The dynamics of the voltage (V) over the capacitor and resistor are determined by the input current (I_{in}) and the current

through the resistor (I_d). A simple analogy for the circuit is that the product concentration in a reaction system is determined by the production rate and the degradation rate. Given constant C and k_{cat} in Eq. 5, the voltage dynamics are thus determined by V_{in} and R which can be translated into biological relevance, as we discuss later. Eqs 1–5 describe the basics of a simple RC circuit and are foundational for understanding the map between circuit modeling and mathematical modeling of kinetic processes. So, we have summarized their derivation in Figure 1.

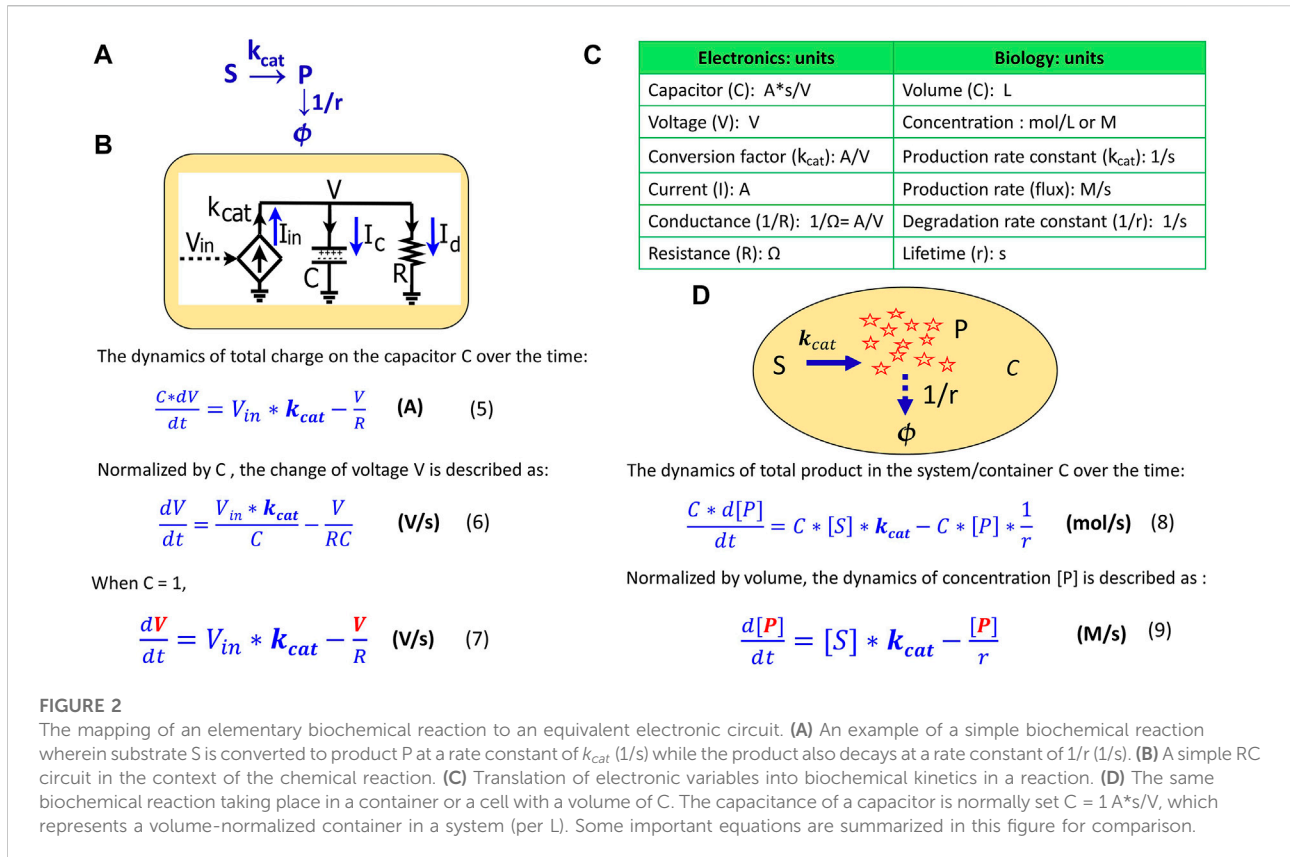
With the voltage dynamics described by Eq. 5, we normalize the equation by C such that the change of V over time is described as:

$$\frac{dV}{dt} = \frac{V_{in} * k_{cat}}{C} - \frac{V}{RC} \quad (6)$$

To simplify the equation, we normally set $C = 1$ (F) = 1 (A*s/V) in circuit modeling and the above equation becomes:

$$\frac{dV}{dt} = V_{in} * k_{cat} - \frac{V}{R} \quad (7)$$

Eq. 7 describes the voltage kinetics in the RC circuit (Figure 1) when $C = 1$. Setting $C = 1$ in circuit models enables a direct map to the mathematics behind the kinetics of a chemical reaction, as we illustrate in Figure 2. In Figure 2A, substrate S is converted into a product P with a production rate constant of k_{cat} (1/s) and the product decays with a rate constant of $1/r$ (1/s). The kinetics of this reaction can be exactly described by an equivalent RC circuit fed by a transconductor (Figure 2B) which is identical to the RC circuit above (Figure 1). In the context of biological systems, we can consider the same reaction taking place in a container or a cell with a volume of C (liter, L) (Figure 2D). According to the law



of mass action in chemistry, the production rate is proportional to the concentration of S and thus is $S * k_{cat}$ (M/s); similarly, the decay rate of the product is $P * (1/r)$ (M/s). The total amount of product P changes over time (mol/s) in the container, and is thus described as below:

$$\frac{C * d[P]}{dt} = C * [S] * k_{cat} - C * [P] * \frac{1}{r} \quad (8)$$

where [S] and [P] are the concentrations (M); C is the container volume (L); k_{cat} and $1/r$ are rate constants (1/s). Eq. 5 is physically parallel to Eq. 8, wherein the former describes the change of the total charge of the capacitor while the latter describes the change of the total amount of product in a container. Then, we normalize Eq. 8 by the container volume C and thus have the concentration kinetics:

$$\frac{d[P]}{dt} = [S] * k_{cat} - \frac{[P]}{r} \quad (9)$$

Eq. 9 describes how the concentration of a product changes over time in a container, a cell, or in any reaction system. When comparing Eq. 9 to Eq. 7, we notice that they become mathematically identical with the input voltage V_{in} representing the substrate concentration [S]; the voltage V

representing the product concentration [P]; k_{cat} , the conversion factor for the current-generating transconductor, representing a production rate constant; and, the resistance R defining the time constant (or lifetime, r) of the product. The side-to-side comparison between electronic dynamics and chemical dynamics for this foundational production reaction is summarized in Figure 2C.

As in this production-reaction example, the dynamics in electronic circuits can be translated into the kinetics of biochemical reactions in more complex systems as well: the voltage (V) corresponds to the concentration (M) of a reagent in a chemical reaction; the current (A) is analogous to a reaction flux (M/s); the resistor R (Ω) defines the degradation of a product, with $1/(RC)$ corresponding to the degradation rate constant and RC corresponding to the equivalent time constant (lifetime); the capacitor with capacitance $C = 1 \text{ (A*s/V)}$ corresponds to a volume-normalized container in a biochemical system (per L). Unless otherwise mentioned, all capacitors in our circuits have $C = 1$. The dynamics of P are determined by the production flux and the degradation flux (Figure 2D) while the dynamics of the voltage (V) in the RC circuit (Figure 2B) are determined by the input source current (I_{in}) and the sink current (I_d).

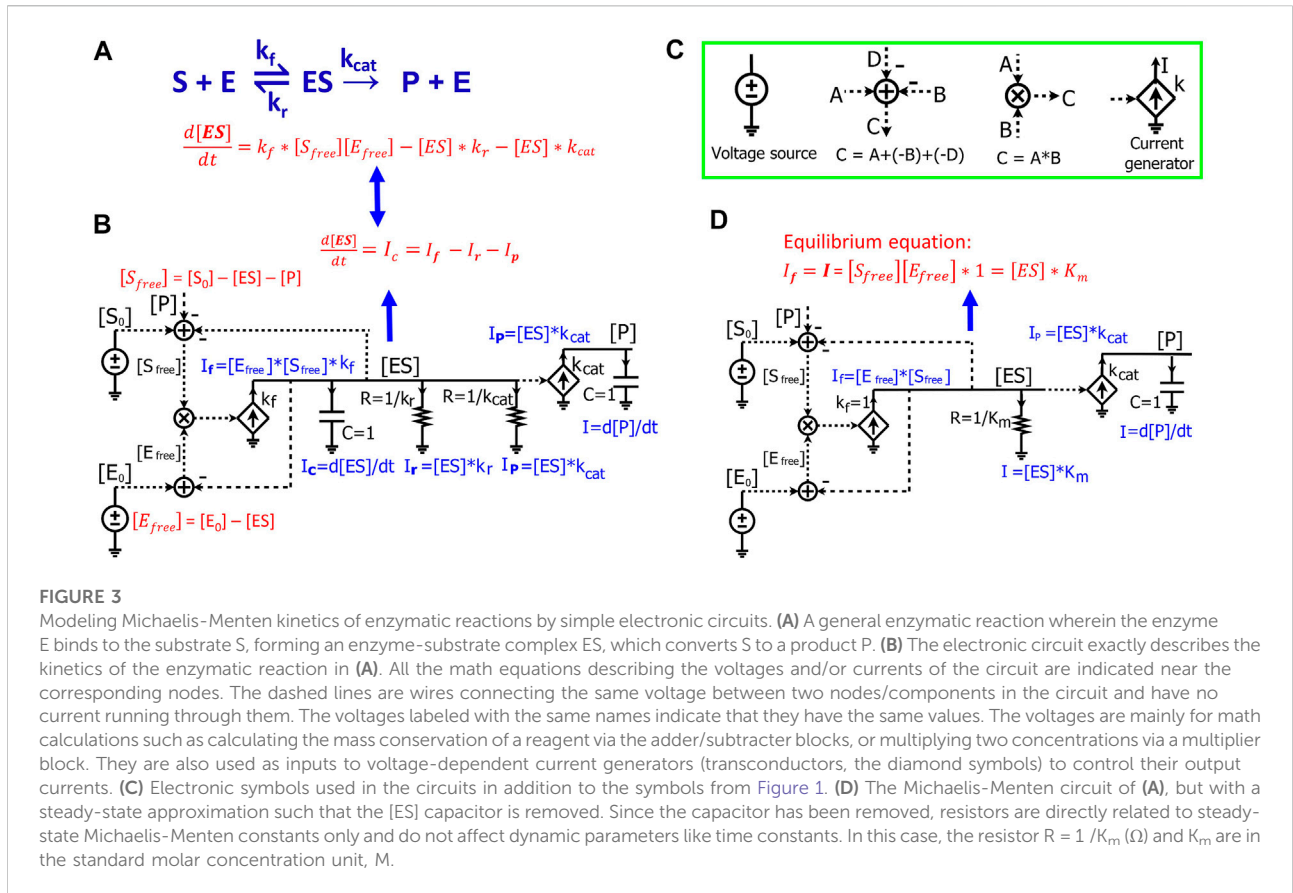


FIGURE 3

Modeling Michaelis-Menten kinetics of enzymatic reactions by simple electronic circuits. (A) A general enzymatic reaction wherein the enzyme E binds to the substrate S, forming an enzyme-substrate complex ES, which converts S to a product P. (B) The electronic circuit exactly describes the kinetics of the enzymatic reaction in (A). All the math equations describing the voltages and/or currents of the circuit are indicated near the corresponding nodes. The dashed lines are wires connecting the same voltage between two nodes/components in the circuit and have no current running through them. The voltages labeled with the same names indicate that they have the same values. The voltages are mainly for math calculations such as calculating the mass conservation of a reagent via the adder/subtractor blocks, or multiplying two concentrations via a multiplier block. They are also used as inputs to voltage-dependent current generators (transconductors, the diamond symbols) to control their output currents. (C) Electronic symbols used in the circuits in addition to the symbols from Figure 1. (D) The Michaelis-Menten circuit of (A), but with a steady-state approximation such that the [ES] capacitor is removed. Since the capacitor has been removed, resistors are directly related to steady-state Michaelis-Menten constants only and do not affect dynamic parameters like time constants. In this case, the resistor $R = 1/K_m$ (Ω) and K_m are in the standard molar concentration unit, M.

2.2 Circuit modeling of Michaelis-Menten kinetics

We next demonstrate how to use circuits to simulate Michaelis-Menten kinetics for enzyme-substrate interactions. For a general enzymatic reaction (Figure 3A), enzyme E binds to a substrate S to form an intermediate enzyme-substrate complex ES at a rate constant of k_f ; ES will then either dissociate into E and S with a reverse rate constant of k_r or be converted to product P and free enzyme E_{free} with a rate constant of k_{cat} . From mass conservation, we have:

$$[E_{free}] = [E_0] - [ES] \tag{10}$$

$$[S_{free}] = [S_0] - [ES] - [P] \tag{11}$$

where $[E_0]$ and $[S_0]$ are the initial concentrations of enzyme and substrate, respectively. The enzyme-substrate complex is converted into product P with a rate proportional to its concentration [ES], such that:

$$\frac{d[P]}{dt} = k_{cat} * [ES] \tag{12}$$

The kinetics of [ES] is determined by three fluxes: the forward reaction rate, $k_f * [E_{free}] * [S_{free}]$, the reversed reaction

rate, $[ES] * k_r$, and the catalytic reaction rate $[ES] * k_{cat}$. Therefore, the dynamics of [ES] are described as below:

$$\frac{d[ES]}{dt} = k_f * [S_{free}] * [E_{free}] - [ES] * k_r - [ES] * k_{cat} \tag{13}$$

The circuit (Figure 3B) exactly represents the enzymatic reaction (Figure 3A). In this circuit, voltages of the wires are labeled with names corresponding to components of the enzymatic reaction. The dashed lines are wires that don't have current going through them but still have the same voltage as the wires or nodes that they originate from. We first derive equations for currents and voltages in the circuit. Since there is no current running through any of the dashed lines/wires, this circuit (Figure 3B) is similar to the circuits we derived above (Figures 1, 2B), consisting of two RC blocks connected together, one with two resistors and the other with no resistors. The dynamics of the voltage [ES] are determined by three currents: I_f , I_r and I_p . Because the voltage across the resistors and capacitor is [ES], by Ohm's law, the current through the resistor ($R = 1/k_r$) is: $I_r = [ES]/R = [ES] * k_r$ which represents the reverse reaction rate/flux; similarly, given the other resistor ($R = 1/k_{cat}$), the current through it is: $I_p = [ES] * k_{cat}$ which represents the catalytic flux; given that the current generator has a conversion factor of k_f and an input voltage $[E_{free}] * [S_{free}]$ that is calculated by the

multiplier, we have the input current $I_f = [E_{free}]^* [S_{free}]^* k_f$. We note that the latter three currents are mathematically exactly the same as the three reaction fluxes in the enzymatic reaction (Eq. 13). Finally, the current through the capacitor is $I_c = \frac{C \cdot d[ES]}{dt} = \frac{d[ES]}{dt}$ (when $C = 1$) (Figure 3B). According to Kirchhoff's current law, the current through the capacitor is given by:

$$\begin{aligned} \frac{d[ES]}{dt} = I_c &= I_f - I_r - I_p \\ &= k_f^* [S_{free}] [E_{free}] - [ES]^* k_r - [ES]^* k_{cat} \end{aligned} \quad (14)$$

Eq. 14 describes the dynamics of the voltage [ES] in the RC circuit (Figure 3B), which is the same as Eq. 13 that we derived from the enzymatic reaction (Figure 3A). Just as in the enzymatic reaction, the dynamics of [ES] are determined by one generation reaction flux and two consumption fluxes (Eq. 13); the dynamics of the voltage [ES] in the RC circuit are determined by one source generation current and two sink consumption currents through the resistors (Eq. 14).

Finally, the voltage [P] is determined by I_p which is generated by a current generator with an input voltage [ES] and a conversion factor of k_{cat} . Since all current generated flows into the capacitor ($C = 1$), we have:

$$I = \frac{C \cdot d[P]}{dt} = \frac{d[P]}{dt} = I_p = k_{cat}^* [ES] \quad (15)$$

Eq. 15 describes the dynamics of the voltage [P] in the RC circuit, which is exactly the same as Eq. 12 that describes the product kinetics in the enzymatic reaction.

In the circuit model (Figure 3B), two adders are used to calculate $[E_{free}]$ and $[S_{free}]$ based on the law of mass conservation. The binding of enzyme and substrate is represented by the multiplier symbol resulting in a signal, $[E_{free}]^* [S_{free}]$, which is the input voltage used to generate current in the first transconductor in Figure 3B. Given the conversion factor of k_f , the resulting current is $[E_{free}]^* [S_{free}]^* k_f$.

Since all the equations describing the electronic circuit and the enzymatic reaction (Figures 3A,B) are mathematically identical, we can directly use the electronic circuit to simulate the kinetics of enzymatic reactions without deriving the underlying equations. The changes of concentrations and reaction fluxes over time are directly mapped to the corresponding changes in voltages and currents, respectively. Therefore, electronic circuits enable a powerful and intuitive method for visualizing multiple math equations in one pictorial schematic. Using these circuits is especially advantageous when one wants to simulate complicated biological pathways/networks where hundreds of differential equations can be represented in a single circuit. To draw/construct and simulate such electronic circuits, multiple electronic software packages are widely and easily available, including Cadence (Cadence Design Systems, Inc.), CircuitLab (<https://www.circuitlab.com/>), or MATLAB

Simulink/Simscape Electrical (The MathWorks, Inc.). Once the circuits are constructed, we can simply run simulations with these tools. The dynamics of the voltages and currents then directly represent real-time changes in the concentrations and reaction fluxes in biochemical reactions, respectively.

The circuit in Figure 3B is an exact circuit for representing biochemical reactions without using any mathematical assumptions/approximations; however, circuit simulation requires known values of k_f and k_r which are not normally available for most enzymatic reactions. To circumvent this requirement and make the circuit more useful in practice, we apply the same assumptions that Michaelis-Menten equation uses to simplify dynamics: Under the quasi steady-state assumption that enzyme-substrate binding is much faster than the substrate-to-product conversion output reaction, the ES concentration is assumed to reach a steady state almost instantaneously. Therefore,

$$\frac{d[ES]}{dt} = k_f^* [S_{free}] [E_{free}] - [ES]^* k_r - [ES]^* k_{cat} = 0 \quad (16)$$

Normalizing the equation by k_f and grouping the [ES] terms, we have:

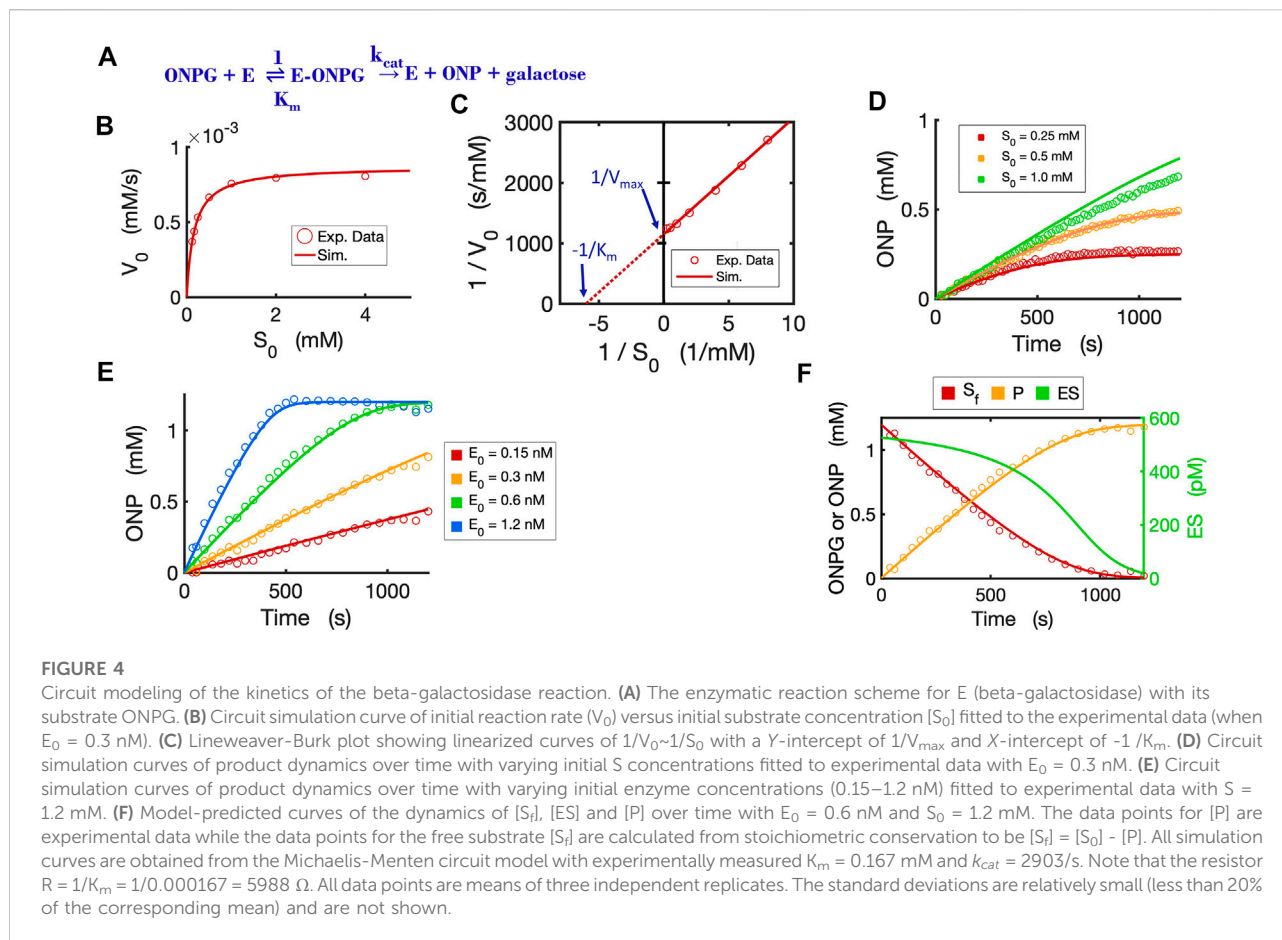
$$[S_{free}] [E_{free}] - [ES]^* (k_r + k_{cat}) / k_f = 0 \quad (17)$$

Letting $K_m = (k_r + k_{cat}) / k_f$, we have the equilibrium equation below:

$$[S_{free}] [E_{free}] = [ES]^* K_m \quad (18)$$

where K_m (M) is the Michaelis-Menten constant. Accordingly, we can also modify the circuit of Figure 3B to reflect the equilibrium Eq. 18. Since it is assumed that [ES] reaches a steady state instantaneously, it means that the capacitor connected to the [ES] voltage node is zero (Figure 3B), architecting an effective RC time constant of zero. Accordingly, we remove the capacitor for [ES] from the circuit in Figure 3B. Next, to normalize both forward and reverse reaction rates by k_f , we set $k_f = 1$ in the circuit. Finally, since we have combined k_f and k_{cat} as in Eq. 17, we merge the two currents, I_r and I_p , into one current ($[ES]^* (k_r + k_{cat}) / k_f$) through a resistor with resistance of $1/K_m$. Therefore, we have a simplified circuit (Figure 3D) containing only the parameters K_m , k_{cat} , S_0 , and E_0 , which are readily available from experiments.

We can easily confirm that the simplified circuit correctly reflects Eq. 18; the forward current generated by the current generator is $I_f = [S_{free}] [E_{free}]$, and the current that goes into the resistor is: $I = [ES]^* K_m$. These two currents are equal since all generated current goes through the resistor. Therefore, we have $I_f = I = [S_{free}] [E_{free}] = [ES]^* K_m$, which is Eq. 18 describing [ES] in the reaction. This simplified circuit (Figure 3D) exactly characterizes the kinetics of the enzymatic reaction (Figure 3A) under the steady-state approximation and is the Michaelis-Menten



equation in the circuit form. This Michaelis-Menten circuit is the basic building block for enzymatic reactions and can be easily extended into more complicated circuits for different mechanisms of enzyme inhibition as we show below. It should be noted that besides ensuring enzyme conservation, i.e., that $[E_{free}]$ and $[ES]$ sum to $[E_0]$, the circuit of Figure 3D also ensures substrate conservation: $[S_{free}] = [S_0] - [ES]$. Ensuring the conservation of both the enzyme and substrate species allows the Michaelis-Menten circuit to be more robust and accurate, especially under scenarios where the enzyme concentration and substrate concentration are comparable (discussed later).

2.3 Circuit modeling of a hydrolytic reaction by beta-galactosidase

To validate the Michaelis-Menten circuit (Figure 3D), we fit our circuit model to experimental data that we collected from an enzyme-substrate reaction. We chose to use a hydrolytic reaction wherein beta-galactosidase is the enzyme and ONPG is the substrate (Figure 4A). We ran the circuit simulation with the four necessary parameters (K_m , k_{cat} , S_0 and E_0), which were all

experimentally determined under our test conditions. As we mentioned above, the reaction flux is given by the current I_p in the circuit while the voltage $[S_0]$ reflects the initial substrate concentration. As expected, the circuit model perfectly matches the measured initial reaction rates when we varied the initial substrate concentrations (Figure 4B). The predicted curve ($V_0 \sim S_0$) is a classic hyperbolic curve for an enzymatic reaction; as S_0 increases the initial reaction rate also increases until it reaches the maximal rate. For Lineweaver-Burk plotting, the circuit model accurately predicts a straight line ($1/V_0$ versus $1/S_0$) with $K_m = 0.167$ mM (derived from the X-intercept in Figure 4C) and $V_{max} = 0.00087$ mM/s (derived from the Y-intercept in Figure 4C) with an excellent fit to the experimental data.

The circuit model can also accurately simulate the time-course dynamics. As shown in Figure 4D, the simulation curves of $[P]$ dynamics fit our experimental data closely under varying initial substrate concentrations. In addition, when we changed the initial concentration of the enzyme with a constant substrate concentration, as expected, the circuit model predicts product dynamics that are in good agreement with our experimental data (Figure 4E). As more enzyme is added, the reaction consumes substrate faster and reaches a plateau sooner. The circuit model

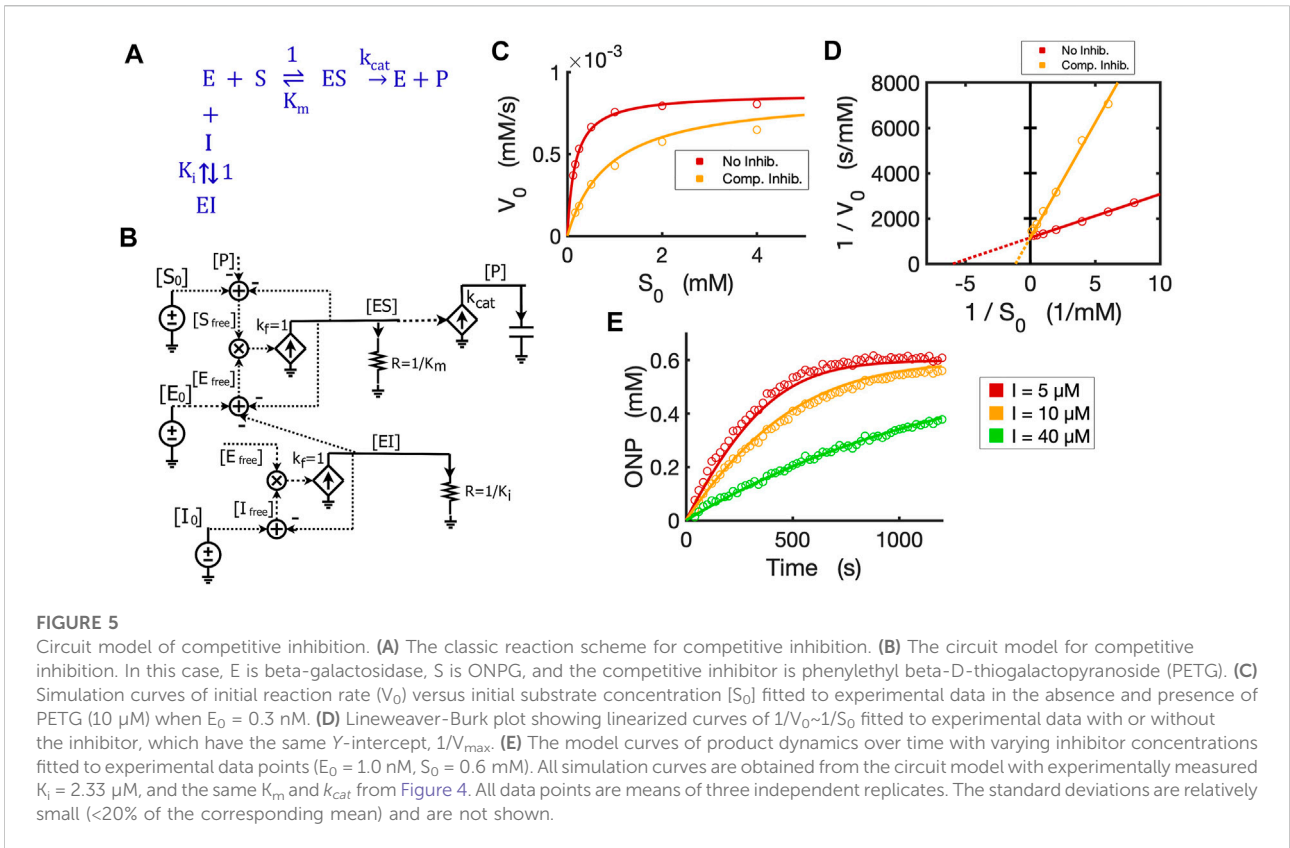


FIGURE 5

Circuit model of competitive inhibition. (A) The classic reaction scheme for competitive inhibition. (B) The circuit model for competitive inhibition. In this case, E is beta-galactosidase, S is ONPG, and the competitive inhibitor is phenylethyl beta-D-thiogalactopyranoside (PETG). (C) Simulation curves of initial reaction rate (V_0) versus initial substrate concentration $[S_0]$ fitted to experimental data in the absence and presence of PETG (10 μM) when $E_0 = 0.3 \text{ nM}$. (D) Lineweaver-Burk plot showing linearized curves of $1/V_0 \sim 1/S_0$ fitted to experimental data with or without the inhibitor, which have the same Y-intercept, $1/V_{\text{max}}$. (E) The model curves of product dynamics over time with varying inhibitor concentrations fitted to experimental data points ($E_0 = 1.0 \text{ nM}$, $S_0 = 0.6 \text{ mM}$). All simulation curves are obtained from the circuit model with experimentally measured $K_i = 2.33 \mu\text{M}$, and the same K_m and k_{cat} from Figure 4. All data points are means of three independent replicates. The standard deviations are relatively small (<20% of the corresponding mean) and are not shown.

also accurately predicts the dynamics of $[S_{\text{free}}]$, $[P]$, and $[ES]$ over time (Figure 4F).

2.4 Circuit modeling of competitive inhibition and product-feedback inhibition

With the basic Michaelis-Menten circuit validated, we developed a circuit model for competitive inhibition. In the classic competitive inhibition model, an inhibitor binds to an enzyme at the substrate-binding site and competes with the substrate for the free enzyme, as shown in the reaction scheme (Figure 5A). To model the competitive inhibition in a circuit, we only need to add an enzyme-inhibitor binding circuit to the same Michaelis-Menten circuit (Figure 3D). Given the assumption that inhibitor binding is also much faster than the catalytic reaction and that the enzyme-inhibitor complex $[EI]$ also, therefore, reaches steady-state instantaneously, we have the equilibrium condition:

$$[I_{\text{free}}][E_{\text{free}}] = [EI] * K_i \tag{19}$$

where K_i is the dissociation constant for the inhibitor. Eq. 19 is similar to Eq. 18, so we make a similar circuit (the lower circuit of

Figure 5B) representing the equilibrium enzyme-inhibitor binding as described in Eq. 19. In this circuit block, all we need is to set $R = 1/K_i$ to reflect the inhibitor binding constant. The voltage $[EI]$ in the circuit is then wired to the $[E_0]$ adder to account for the consumption of free enzyme that has been competitively bound by the inhibitor. Therefore, we have a competitive inhibition circuit model (Figure 5B). We used a competitive inhibitor of beta-galactosidase and experimentally demonstrated that this circuit is identical to the classic equations describing the kinetics of competitive inhibition. The circuit model accurately predicts the relationship between initial reaction rates and initial substrate concentrations ($V_0 \sim S_0$) in the presence and absence of the inhibitor (Figure 5C). As $[S_0]$ increases, the initial reaction rate V_0 also increases and eventually will reach the same maximal rate V_{max} even in the presence of the inhibitor. The linearized curves (Lineweaver-Burk plot) show the expected behavior of competitive inhibition where the inhibitor increases the apparent K_m but not the maximal reaction rate (V_{max}) (Figure 5D). In addition, the circuit model can also exactly predict the product dynamics over time under different inhibitor concentrations (Figure 5E). Thus, using our experimental data, we have verified that the circuit model accurately describes the kinetics for competitive inhibition.

The circuit for competitive inhibition is a useful building block and can be used to construct circuits for complicated

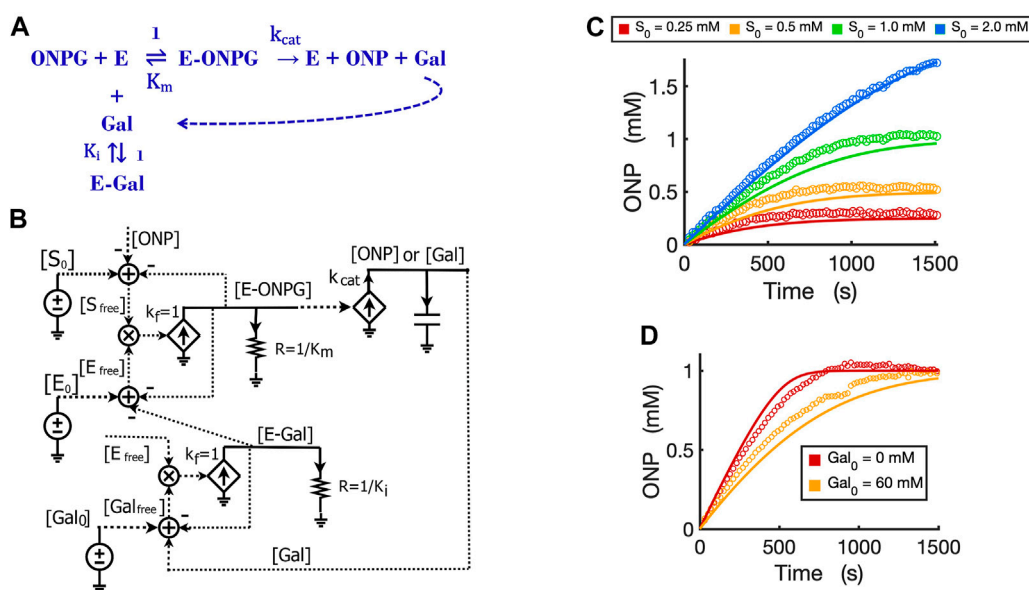


FIGURE 6

Circuit modeling of product feedback inhibition. (A) The scheme of product feedback inhibition based on competitive inhibition. Galactose [Gal] is one of the products and is also an inhibitor to the enzyme, beta-galactosidase. (B) The circuit model for product feedback inhibition: $[S_0]$ is the initial ONPG added to the reaction while $[Gal_0]$ is the initial galactose added to the reaction. (C) Model curves of product dynamics over time fitted to experimental data with varying initial substrate concentrations (when $[Gal_0] = 40$ mM, $E_0 = 0.7$ nM). (D) Model curves of product dynamics fitted to experimental data with or without galactose added to the reaction (when ONPG = 1 mM, $E_0 = 0.85$ nM). All simulation curves are obtained from the circuit model (B) with experimentally measured $K_i = 13.7$ mM, and the same K_m and k_{cat} from Figure 4. All data points are means of three independent replicates with standard deviations less than 20% of the corresponding mean (not shown).

biological pathways when there are competitive inhibitors involved. As an example, we now use the competitive inhibition circuit (Figure 5B) to model the kinetics of product inhibition in an enzymatic reaction. Product inhibition is a common way to regulate reaction rates in metabolic pathways. Based on previous reports that beta-galactosidase can be competitively inhibited by a relatively high concentration of its own product galactose (Portaccio et al., 1998; Nguyen et al., 2006), we easily construct a reaction scheme for the product inhibition wherein the product galactose competes for the free enzyme (Figure 6A): In Figure 5B, we simply replace the inhibitor I_0 with product $[Gal_0]$ that can be externally added to the reaction and also wire newly produced $[Gal]$ to the total product pool to architect the feedback inhibition; the resultant circuit is shown in Figure 6B.

It is worth noting that simple rewiring and reuse of circuit building blocks avoids the need for any math equations, and preserves physical and chemical intuition. We can directly and rapidly map the reaction mechanism of Figure 6A to a quantitatively accurate representation of its function and dynamics in Figure 6B. The implicit (caused by subtractive inputs from the “use-it-and-lose-it” mass conservation in Figures 4–6) and explicit (due to product inhibition) feedback loops are all evident and clearly represented.

We validated the product-inhibition circuit model by fitting it to experimental data. The circuit model shows good fits to the experimental data for product dynamics over time when varying substrate concentrations were added but with constant galactose concentration (Figure 6C). In another experiment, we compared the reactions with and without the product galactose added before starting the reaction. As expected, when the initial amount of galactose is added, the reaction is inhibited and takes a longer time to reach a plateau wherein all substrate has been consumed (Figure 6D).

2.5 A generalized molecular-binding circuit block for enzyme inhibition and two-substrate reactions

We next sought to develop a generalized circuit model for all types of enzyme inhibition including competitive, non-competitive, and uncompetitive inhibition. In the generalized reaction scheme (Figure 7A), the enzyme forms ES, EI, and ESI complexes with the substrate, inhibitor, or both, respectively; the specific reaction fluxes can be derived from the corresponding rate constants. We can directly translate the reaction scheme into an equivalent circuit (Figure 7B) that exactly describes all the dynamics of each species in the reaction and has identical math

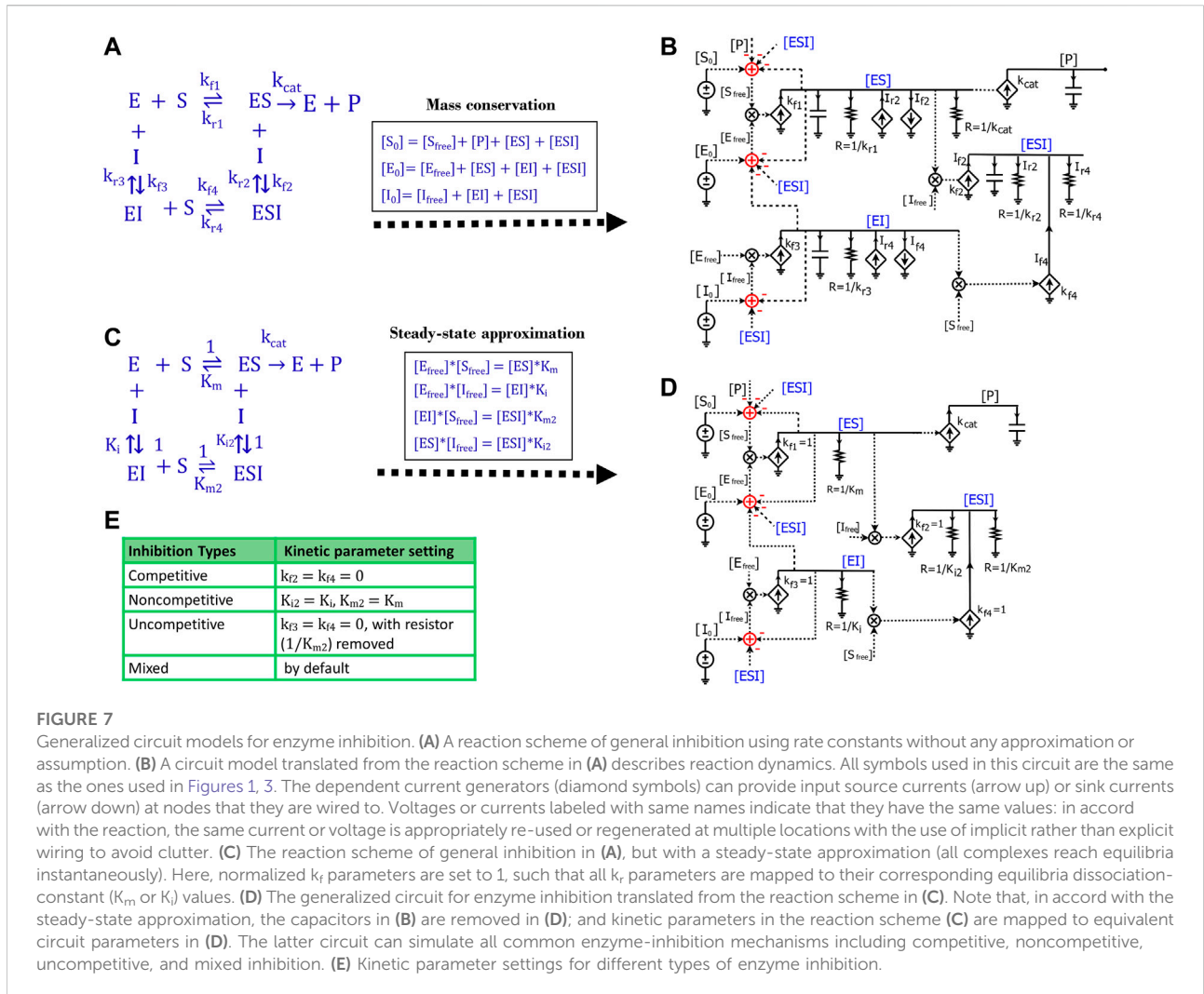


FIGURE 7

Generalized circuit models for enzyme inhibition. (A) A reaction scheme of general inhibition using rate constants without any approximation or assumption. (B) A circuit model translated from the reaction scheme in (A) describes reaction dynamics. All symbols used in this circuit are the same as the ones used in Figures 1, 3. The dependent current generators (diamond symbols) can provide input source currents (arrow up) or sink currents (arrow down) at nodes that they are wired to. Voltages or currents labeled with same names indicate that they have the same values: in accord with the reaction, the same current or voltage is appropriately re-used or regenerated at multiple locations with the use of implicit rather than explicit wiring to avoid clutter. (C) The reaction scheme of general inhibition in (A), but with a steady-state approximation (all complexes reach equilibria instantaneously). Here, normalized k_r parameters are set to 1, such that all k_r parameters are mapped to their corresponding equilibria dissociation-constant (K_m , or K_i) values. (D) The generalized circuit for enzyme inhibition translated from the reaction scheme in (C). Note that, in accord with the steady-state approximation, the capacitors in (B) are removed in (D); and kinetic parameters in the reaction scheme (C) are mapped to equivalent circuit parameters in (D). The latter circuit can simulate all common enzyme-inhibition mechanisms including competitive, noncompetitive, uncompetitive, and mixed inhibition. (E) Kinetic parameter settings for different types of enzyme inhibition.

equations, as we derive below. Based on the mass conservation law, we have the following relationships for $[S_0]$, $[E_0]$ and $[I_0]$ (Figure 7A):

$$[S_0] = [S_{free}] + [P] + [ES] + [ESI] \quad (20)$$

$$[E_0] = [E_{free}] + [ES] + [EI] + [ESI] \quad (21)$$

$$[I_0] = [I_{free}] + [EI] + [ESI] \quad (22)$$

Such mass conservation is represented in the equivalent circuit (Figure 7B) by an adder block with a positive conserved total species input (S_0 , E_0 , or I_0); subtractive (negative) inputs are caused by the use of the species (for binding or product transformation) to generate other species (P , ES , EI , or ESI); finally, free variables (S_{free} , E_{free} , or I_{free}) are the resulting outputs of the adder blocks. The subtractive inputs always cause the ‘use-it-and-lose-it’ implicit negative-feedback loops in chemical reaction networks (Teo et al., 2015; Teo and

Sarpeshkar, 2020). As shown in Figure 7A, the dynamics of $[ES]$ are determined by five reaction fluxes, including two generation fluxes and three consumption fluxes. Therefore, we have:

$$\begin{aligned}
 \frac{d[ES]}{dt} = & k_{f1} * [S_{free}] [E_{free}] + [ESI] * k_{r2} - [ES] * k_{r1} \\
 & - [ES] [I_{free}] * k_{f2} - [ES] * k_{cat}
 \end{aligned} \quad (23)$$

Likewise, the voltage dynamics of $[ES]$ in the circuit (Figure 7B) are also determined by five currents/fluxes. The two generation fluxes include the forward reaction flux, $k_{f1} * [S_{free}] [E_{free}]$ for enzyme-substrate binding indicated by the k_{f1} current source, and the reverse reaction flux (I_{r2}), $[ESI] * k_{r2}$ from $[ESI]$, indicated by the I_{r2} current source; the three consumption fluxes include the dissociation reaction flux, $[ES] * k_{r1}$, indicated by the $1/k_{r1}$ resistor, the reaction flux for ES and inhibitor binding (I_{f2}), $[ES] [I_{free}] * k_{f2}$, indicated by the I_{f2} sink current source, and the catalytic reaction flux, $[ES] * k_{cat}$.

The dynamics of $[EI]$ are determined by two generation fluxes and two consumption fluxes in the reaction scheme (Figure 7A). Therefore, we have:

$$\frac{d[EI]}{dt} = k_{f3} * [I_{free}] [E_{free}] + [ESI] * k_{r4} - [EI] * k_{r3} - [EI] * [S_{free}] * k_{f4} \quad (24)$$

Similarly, in the circuit (Figure 7B), the voltage dynamics of $[EI]$ are also determined by two source currents and two sink currents. Two supply currents include $k_{f3} * [I_{free}] [E_{free}]$, indicated by the k_{f3} current source, and the dissociation flux (I_{r4}), $[ESI] * k_{r4}$, indicated by the I_{r4} current source. The two sink currents include the current through the resistor ($1/k_{r3}$), $[EI] * k_{r3}$, and the current through the I_{f4} current source, which is $[EI] * [S_{free}] * k_{f4}$.

The dynamics of $[ESI]$ in the reaction scheme (Figure 7A) are quantified by two generation fluxes and two consumption fluxes, so we have:

$$\frac{d[ESI]}{dt} = k_{f2} * [ES] [I_{free}] + k_{f4} * [EI] [S_{free}] - [ESI] * k_{r2} - [ESI] * k_{r4} \quad (25)$$

This equation is also exactly reflected by the voltage dynamics of $[ESI]$ in the circuit (Figure 7B), which are determined by two source currents and two sink currents. As shown in the circuit, the two source currents include one from the k_{f2} current source, $k_{f2} * [ES] [I_{free}]$, and one from the k_{f4} current source, $k_{f4} * [EI] [S_{free}]$. The two sink currents are indicated by two resistors $1/k_{r2}$ and $1/k_{r4}$, with quantities of $[ESI] * k_{r2}$, and $[ESI] * k_{r4}$, respectively (Figure 7B).

Finally, the product $[P]$ dynamics that are described by Eq. 12 are also described by the dynamics of voltage $[P]$ in the circuit (Figure 7B). As illustrated above, Eqs 12 and 20–25 describing the reaction kinetics/dynamics for the reaction scheme (Figure 7A) are exactly mapped to a single circuit (Figure 7B). Given the rate constants and initial conditions, these equations (Eqs 12 and 20–25) can be solved by running simulations of the circuit. In short, this circuit not only accurately visualizes all differential equations in one diagram but can also easily provide solutions to these equations via simulations of the circuit.

Since we haven't applied any assumptions while deriving the equations or in developing the circuit (Figures 7A,B), this circuit is very general and can be used to model the kinetics of any reaction with the same topology. However, we need to know the values of all the rate constants to run the simulation of this circuit, which is not very convenient. To make the circuit more useful in practice, we simplified the reaction by applying the steady-state approximation (Figure 7C), which is also used in the derivation of enzyme inhibition kinetics from the Michaelis-Menten equation. Under this approximation, substrate binding and inhibitor binding to an enzyme are viewed as instantaneous (much faster than the catalytic reaction) and thus all intermediate

complexes reach quasi-steady states. Therefore, we have the equilibrium equations below:

$$[E_{free}] * [S_{free}] = [ES] * K_m \quad (26)$$

$$[E_{free}] * [I_{free}] = [EI] * K_i \quad (27)$$

$$[EI] * [S_{free}] = [ESI] * K_{m2} \quad (28)$$

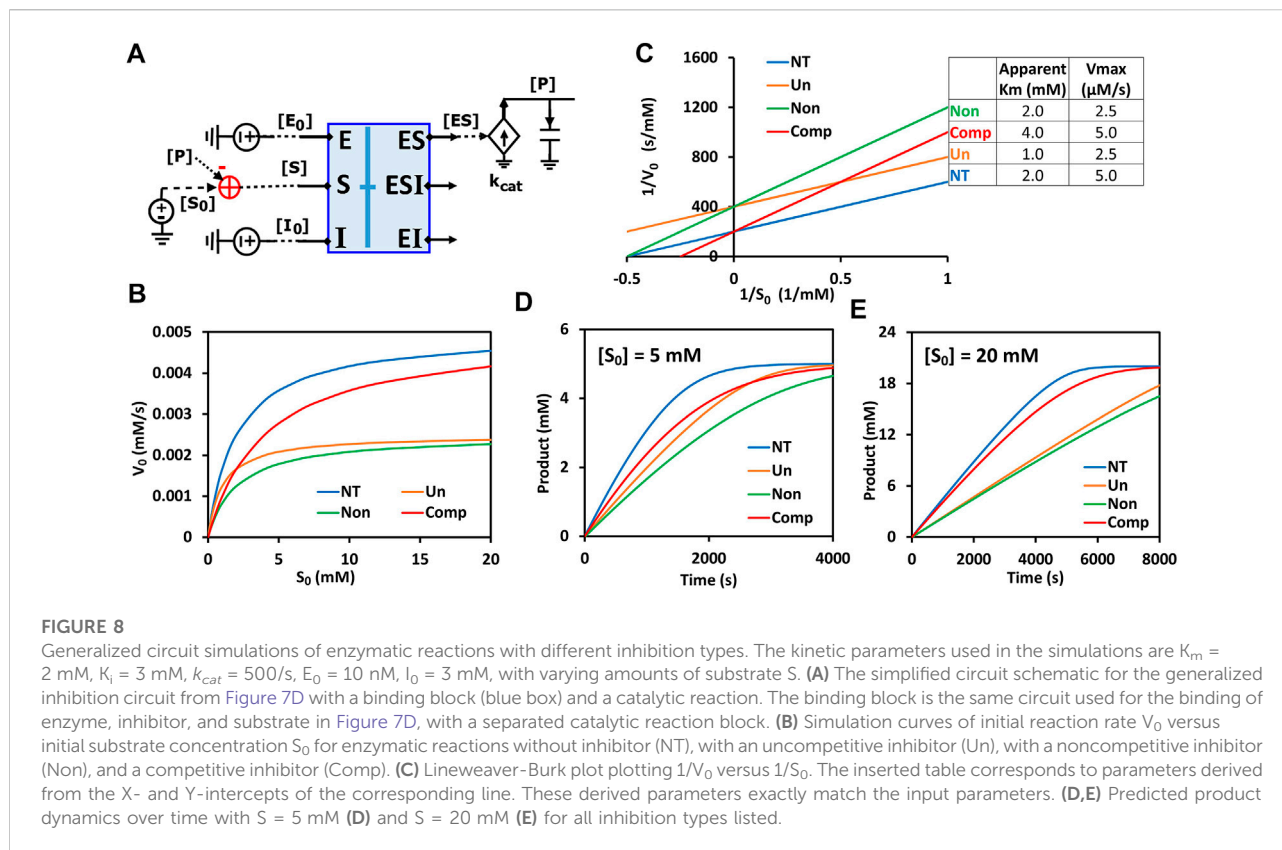
$$[ES] * [I_{free}] = [ESI] * K_{i2} \quad (29)$$

Similar to the tactics used to derive the Michaelis-Menten circuit (Figure 3D), these equilibrium equations are reflected in the circuit (Figure 7D) by removing all capacitors, setting all four k_f values equal to 1, and combining currents for each complex into one or two resistors. We thus achieve a parameter-reduced circuit generalized for enzymatic reactions with inhibition (Figure 7D). Note that ESI has two production fluxes, one from ES and the other from EI, and two consumption fluxes, dissociation from ESI to EI and to ES, respectively. We can sum Eqs 28, 29, and have Eq. 30 which determines the steady state of $[ESI]$:

$$[EI] * [S_{free}] + [ES] * [I_{free}] = [ESI] * (K_{m2} + K_{i2}) \quad (30)$$

Accordingly, Eq. 30 is also reflected in the circuit (Figure 7D) for the voltage of $[ESI]$, which is determined by two source currents and two sink currents through the two resistors. The two source currents are provided through the k_{f2} current source and k_{f4} current source; the two sink currents are realized by the $1/K_{m2}$ resistor and $1/K_{i2}$ resistor, respectively.

Based on the mathematical derivations above, we have developed a parameter-reduced circuit (Figure 7D) generalized for all four kinds of enzyme inhibition including competitive, non-competitive, uncompetitive, and mixed inhibition. By default, the generalized circuit (Figure 7D) can be viewed as a circuit model for mixed inhibition while the other three types of inhibition are just special cases. For competitive inhibition, since there is only one $[EI]$ reaction (Figure 7C), setting the parameters $k_{f2} = k_{f4} = 0$ gives $[ESI] = 0$ and the circuit (Figure 7D) becomes the same circuit in Figure 5B for competitive inhibition. For non-competitive inhibition, the inhibitor binds to the enzyme at a different site from the catalytic site and this binding is independent of the substrate binding, resulting in $K_{m2} = K_m$ and $K_{i2} = K_i$ in the reaction scheme (Figure 7C). Consequently, using those same settings in the circuit (Figure 7D), we have the circuit for non-competitive inhibition. Since non-competitive inhibition is a special case of mixed inhibition, when there are no special requirements on K_{i2} and K_{m2} , the circuit (Figure 7D) by itself is a model for mixed inhibition. For uncompetitive inhibition, there is only one production flux for ESI (from ES), meaning that $k_{f3} = k_{f4} = 0$ in the circuit (Figure 7D). As a result, there is only one consumption flux for $[ESI]$ in the uncompetitive inhibition circuit, such that there is only current through the resistor ($R = 1/K_i$), achieved by either removing the other resistor

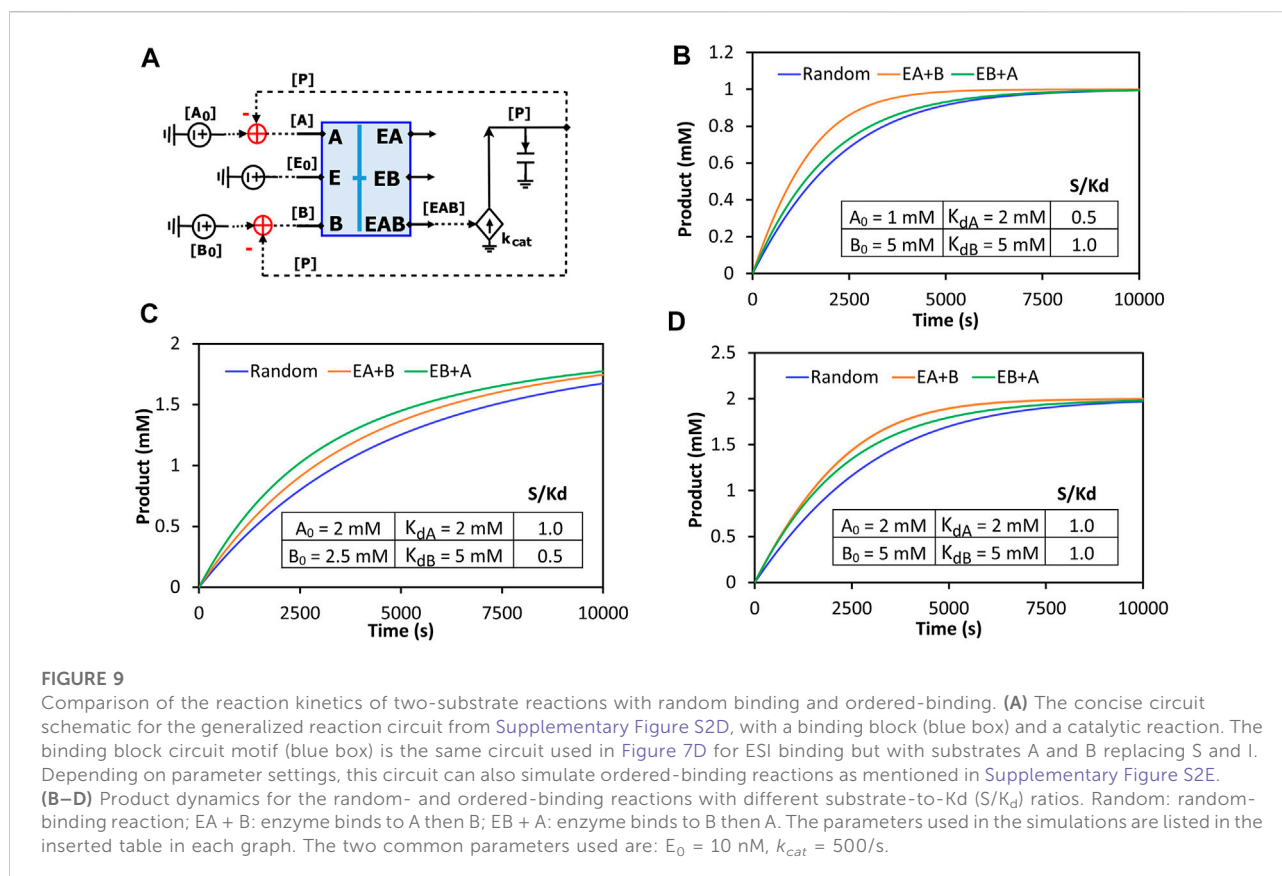


$R = 1/K_m$ or setting its resistance to a huge value such that the current running through it can be ignored. In summary, we have developed a generalized circuit for four types of enzyme inhibition. Its simulation requires five parameters (K_m , k_{cat} , K_i , K_{m2} and K_{i2}) for modeling mixed inhibition and only three kinetic parameters, K_m , k_{cat} , and K_i , for modeling competitive, non-competitive, or uncompetitive inhibition.

The generalized circuit (Figure 7D) consists of two parts: a binding block and a catalytic reaction block. The binding block is the circuit representing the binding of enzyme-substrate (ES), enzyme-inhibitor (EI), and enzyme-substrate-inhibitor (ESI) in Figure 7D. Since the binding circuit can fundamentally simulate different bindings among biomolecules, it is a useful building block for modeling more complicated interactions. Therefore, we extracted the binding block and rearranged the generalized circuit (Figure 7D) into a more concise schematic symbol (Figure 8A) for easy visualization. The new circuit consists of a binding block (blue box) and a catalytic reaction block (Figure 8A), describing exactly the same kinetics/dynamics as in the original circuit (Figure 7D). This binding block has three inputs ($[E_0]$, $[S_0]$, and $[I_0]$) and three outputs ($[ES]$, $[EI]$, and $[ESI]$), which are the same as those in Figure 7D. The reaction block is separated; hence there is product $[P]$ feedback to the substrate input to maintain mass conservation of S as shown in Figure 8A. With all the underlying schematic circuits built within

it (Figure 7D), our binding-block circuit motif symbol is convenient to use: As in highly complex electronic integrated-circuit design with hierarchical building blocks, it provides a useful visualization aid; it can be repeatedly instantiated to create ever-more complex biochemical reaction networks.

To verify that our generalized circuit can accurately simulate all enzyme inhibition types, we ran simulations with the circuit using the same kinetic parameters (K_m , k_{cat} , and K_i) and initial concentrations of enzyme, substrate, and inhibitor for all of its special cases, i.e., for competitive, noncompetitive, and uncompetitive inhibition. As expected, our circuit model predicted the characteristic curves for the relationship between $[S_0]$ and initial reaction rate V_0 for all three inhibition types (Figure 8B). Lineweaver-Burk plotting further confirmed that our circuit model is accurate (Figure 8C): For competitive inhibition, the apparent K_m increases but V_{max} remains the same upon the addition of the inhibitor; for non-competitive inhibition, the V_{max} decreases but apparent K_m remains the same; for uncompetitive inhibition the apparent K_m and V_{max} both decrease with the same proportion such that the curve's slope (K_m/V_{max}) without inhibitor (NT, the blue line in Figure 8C) is identical to that with inhibitor (Un, the orange line in Figure 8C). Furthermore, this circuit can also simulate mixed inhibition where K_m , K_{m2} , K_i , and K_{i2} are independent of each other, the most general case. As an example, when using the



same K_m and K_i values as in Figure 8 but setting $K_{i2} = 6$ mM and $K_{m2} = 4$ mM, we obtain a typical curve for mixed inhibition with different X- and Y-intercepts on the Lineweaver-Burk plot (Supplementary Figure S1).

Remarkably, this circuit shows that the time-course dynamics of the product differ greatly amongst the three inhibition types (Figures 8D,E) and that the difference depends on substrate concentration: When $S = 5$ mM, the product dynamics of uncompetitive inhibition are similar to that of competitive inhibition (Figure 8D), while when $S = 20$ mM the product dynamics of uncompetitive inhibition are closer to that of noncompetitive inhibition (Figure 8E). Non-competitive inhibition usually has the strongest inhibition among the three types, with the slowest product production (Figures 8B,D,E). Our simulation results suggest that, to obtain accurate molecular kinetics, it is important to choose the right inhibition mechanism when constructing models. Choosing the right type of inhibition is especially critical for cascade reactions such as in metabolic pathways where there are many steps with feedback inhibition caused by the final product and/or intermediate metabolites.

The binding block circuit motif (Figures 7D, 8A) is very useful and versatile for different applications. As another example, we used the same binding block and made a circuit

to simulate reactions with two substrates binding to the same enzyme. There are three possibilities of binding order: Enzyme binds to A and then to B; Enzyme binds to B and then to A; Enzyme binds to A and B randomly. We called the first two “ordered-binding reactions” and the last one “random-binding reaction”. The reaction schemes and a circuit model for a generalized reaction are demonstrated in Supplementary Figure S2. Our circuit simulations clearly show that the binding order can cause different reaction dynamics. Normally, the random-binding reaction has the slowest rate while the rate for ordered-binding reactions depends on the substrate-to- K_d ratio (S/K_d) (Figure 9). Given the same concentration of substrate A and B, the reaction is faster when the enzyme first binds to B (greater K_d and thus smaller S/K_d) while given the same K_d for both substrates, the reaction is faster when the enzyme first binds to A (lower concentration and thus smaller S/K_d) (Supplementary Figure S3). Indeed, when we vary the S/K_d ratio for both substrates, the reaction is always faster when the enzyme first binds to the substrate with the smaller S/K_d (Figure 9). It is interesting to point out that given the same S/K_d ratio (1:1 in Figure 9D), the rates are initially similar for both ordered-binding reactions but as two substrates are consumed to cause one to have smaller S/K_d (substrate A in Figure 9D), the reaction (with A binding first) is eventually faster

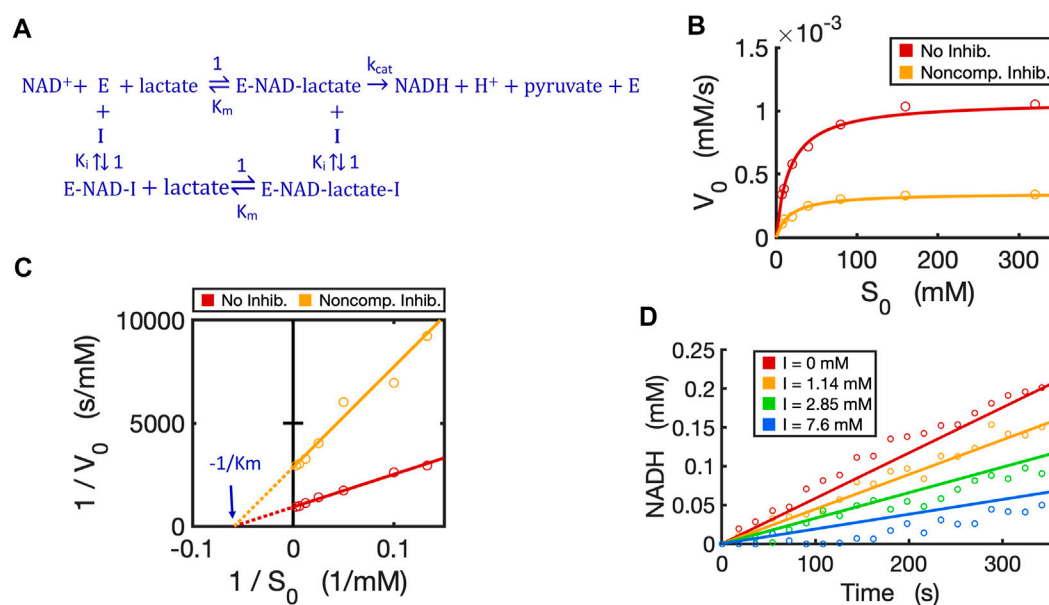


FIGURE 10

Circuit modeling of non-competitive inhibition of LDH by oxamate. (A) The reaction scheme of non-competitive inhibition against LDH, where the inhibitor I is oxamate. For simplification, the initial catalysis can be viewed as a directional reaction, though the LDH reaction is known to be reversible; the fast binding step of NAD^+ to enzyme is neglected in this reaction scheme. (B) Simulation curves of V_0 versus S_0 fitted to measured experimental data in the absence and presence of oxamate (7.6 mM), when $E_0 = 5.0$ nM. (C) Lineweaver-Burk plot showing linearized curves of $1/V_0$ versus $1/S_0$ with and without the inhibitor, which have the same X-intercept of $-1/K_m$. (D) The model curves of product dynamics over time with varying inhibitor concentrations fitted to experimental data points (when $S = 80$ mM, $E_0 = 3.3$ nM). All simulation curves are obtained from the circuit model (Figures 7D, 8A) with experimentally measured $K_m = 17.1$ mM, $k_{cat} = 215.5$ (1/s), and $K_i = 3.66$ mM. All data points are means of three independent replicates with standard deviations less than 20% of the corresponding mean (not shown).

than the reaction with the opposite binding order. Given that the binding order matters for reaction kinetics, modelers may need to carefully select which binding order best approximates the reaction they are modeling.

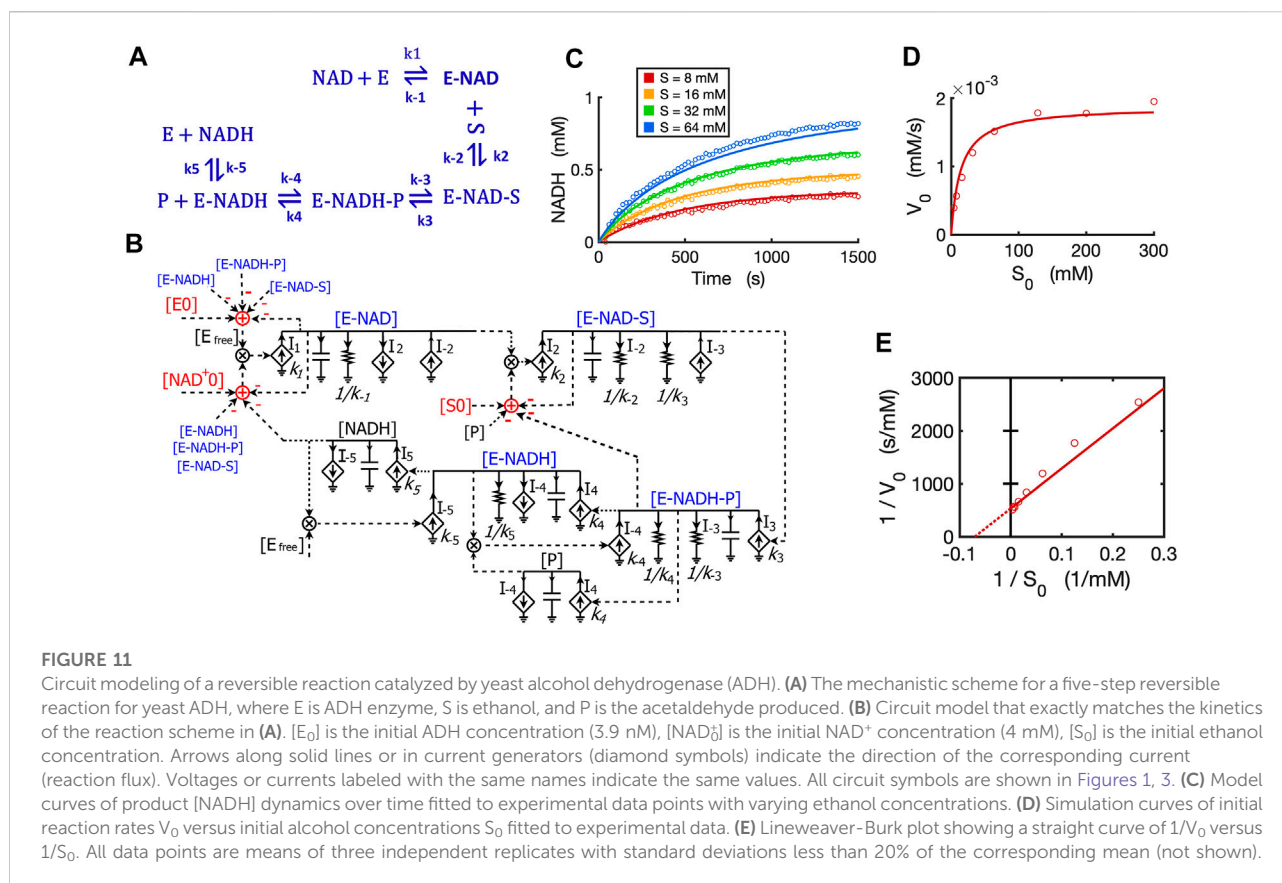
2.6 Circuit modeling of non-competitive inhibition

We have now verified in theory that the generalized circuit (Figure 8A) is accurate in predicting kinetics for all enzyme inhibition types. This circuit is also convenient to use; with inputs of K_m , k_{cat} and K_i as well as experimental initial conditions, running simple simulations can provide all kinetic data, which can be compared to experimentally measured data. As an example, we now use our circuit to model the noncompetitive inhibition wherein lactate oxidation by lactate dehydrogenase is inhibited by a noncompetitive inhibitor, oxamate (Powers et al., 2007). In this redox reaction (Figure 10A), we varied the concentration of lactate while keeping a constant NAD^+ concentration. As expected, the circuit-predicted curves capture the experimental data nicely. The initial reaction rate increases as substrate concentration increases, but, in the presence of the noncompetitive inhibitor, the reaction rate

never approaches the V_{max} of the reaction when without the inhibitor (Figure 10B). Linearized curves from Lineweaver-Burk plots show that noncompetitive inhibition has the same K_m as the reaction without the inhibitor, but a smaller V_{max} (i.e., greater $1/V_{max}$) (Figure 10C). The generalized circuit can also simulate the time-course kinetics of NADH production for the initial period (the first 360s) (Figure 10D) where the catalytic reaction can be largely viewed in the forward direction.

2.7 Circuit modeling of reversible reactions

We developed a circuit to simulate reversible reactions because they are very common in metabolic pathways. Since the kinetic mechanism for the reversible reaction of alcohol dehydrogenase (ADH) is well studied with all rate constants known (Dickinson and Dickenson, 1978; Ganzhorn et al., 1987; Plapp, 2010), we developed a circuit model for this reversible reaction with ethanol and NAD^+ both as substrates. The kinetics of this reaction by yeast ADH follow the ordered Bi-Bi mechanism, resulting in a five-step reversible reaction (Ganzhorn et al., 1987) as shown in Figure 11A. First, NAD^+ binds to the enzyme ADH and forms an E-NAD complex; the substrate ethanol then binds to E-NAD and forms an

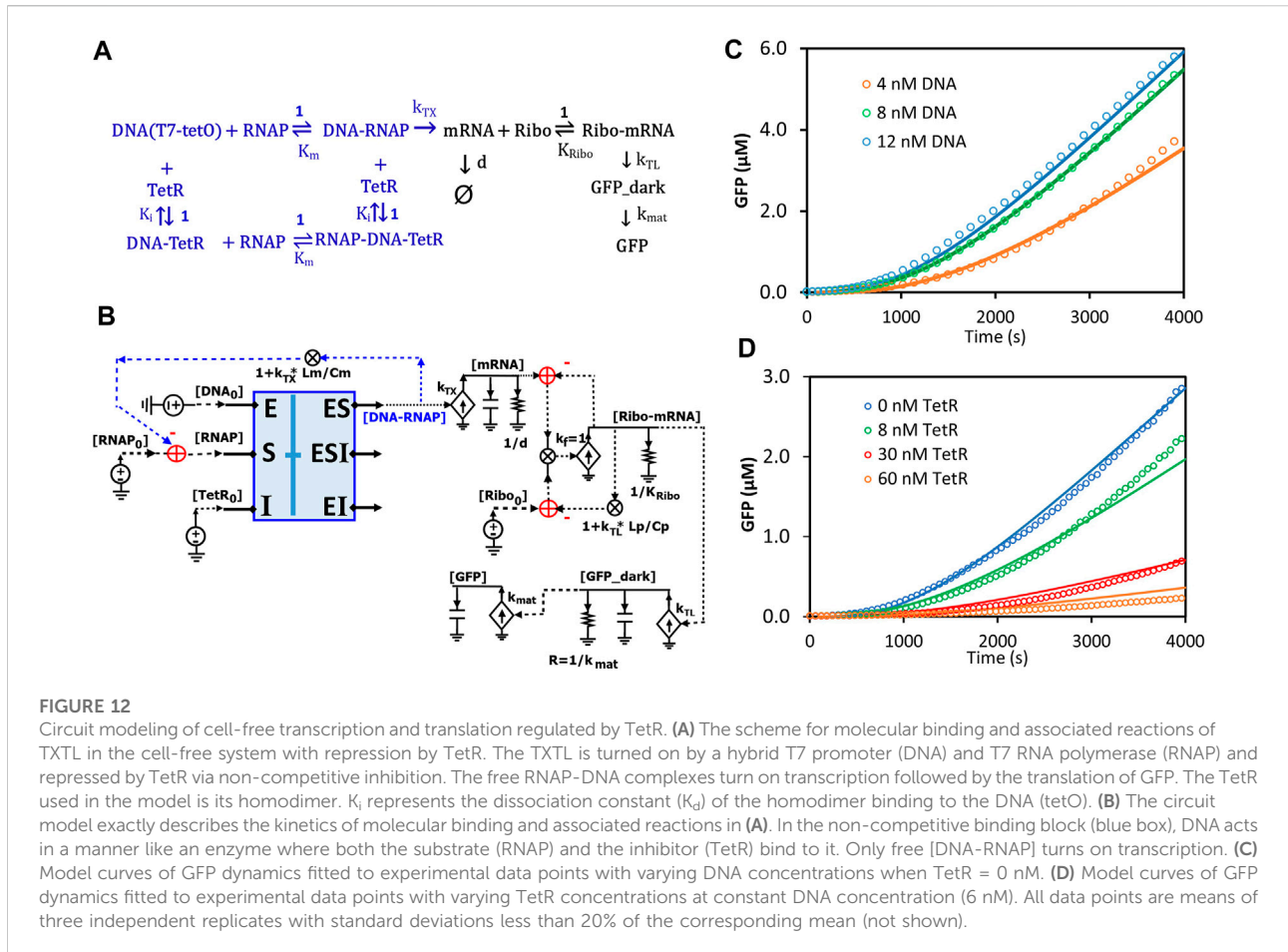


E-NAD-S complex; this complex turns into a new complex E-NADH-P and then the first product aldehyde (P) releases, resulting in an E-NADH complex; the last step is the dissociation of NADH from the enzyme. The total reaction consists of five reversible steps, each with forward and reverse rate constants as indicated in the reaction scheme (Figure 11A).

To mathematically simulate the dynamics/kinetics of all species in this multi-step reaction would require a long list of differential equations as well as many mass conservation equations. Instead, we can simply translate the reaction scheme into a single circuit (Figure 11B) without deriving differential equations. The circuit model is constructed by using a circuit block similar to the one for the enzyme-substrate circuit (Figure 3B). The difference is that each intermediate complex (blue text) including E-NAD, E-NAD-S, E-NADH-P, and E-NADH in steps 1–4 has two production fluxes and two consumption fluxes (Figure 11B), instead of only three fluxes for the $[ES]$ complex in the circuit (Figure 3B) for classic Michaelis-Menten kinetics without a reversible catalytic reaction. It should be noted that the product aldehyde $[P]$ is produced in proportion to $[E-NADH-P]$ with a rate constant of k_4 while it is consumed by binding back to $[E-NADH]$, forming

$[E-NADH-P]$ with a rate constant k_4 , resulting in a reaction rate of $I_4 = k_4 \cdot [P] \cdot [E-NADH]$. Similarly, another product $[NADH]$ is produced in proportion to $[E-NADH]$ with a reaction rate of $k_5 \cdot [E-NADH]$ while it is also consumed by binding back to the enzyme, forming $[E-NADH]$ with a rate of $I_5 = k_5 \cdot [NADH] \cdot [E_{free}]$. Another important note is that the conservations of enzyme, NAD^+ , and ethanol (S) during the reaction are indicated by adder and subtraction symbols in red in the circuit (Figure 11B).

To verify the accuracy of our circuit model, we fit experimental data for $[NADH]$ produced from ethanol oxidation by ADH for varying amounts of alcohol and a fixed concentration of initial NAD^+ . Given that the 10 rate constants for the whole reaction are known from previous studies (Dickinson and Dickenson, 1978; Ganzhorn et al., 1987), we used these kinetic parameters as input to our circuit model. We were able to get a good fit with only some adjustments (Supplementary Table S1) relevant to our specific experimental conditions. Our circuit model can accurately simulate the product dynamics over time with varying amounts of ethanol input (Figure 11C). Importantly, our circuit model also correctly predicts the classic relationship between initial reaction rates (V_0) and initial ethanol



concentrations (S_0) based on modeling the initial 60 s of the reaction (Figure 11D). The Lineweaver-Burk plot shows a straight line for $1/V_0$ versus $1/S_0$, which captures our data closely (Figure 11E). From the X- and Y-intercepts, we calculated a K_m of 14.3 mM for ethanol and k_{cat} of 483/s, which agrees well with previous reports (Ganzhorn et al., 1987).

2.8 Circuit modeling of transcription and translation in a cell-free system

Circuits can be used to model any biological system, not just enzymatic reactions (Sarpeshkar, 2010; Teo and Sarpeshkar, 2020). Here, we sought to model transcription and translation (TXTL) kinetics regulated by TetR in an *E. coli*-based cell-free system. In this system, the DNA insert region (a hybrid T7 promoter regime) on a plasmid (DA313) has a T7 RNAP binding site and a TetR binding site (tetO) that is 5-bp downstream; given the relatively small sizes of T7RNAP and TetR, the DNA region acts like an enzyme capable of binding both the “substrate” (T7 RNAP) and the inhibitor protein (TetR) at two different sites. Since T7 RNAP

and the inhibitor TetR bind to the DNA regime (“enzyme”) at two different sites, we can assume their interactions to architect noncompetitive binding (Figure 12A). Such transcriptional binding is similar to the noncompetitive binding/reaction scheme (Figures 7C,D, 8A) but with the difference that none of the “substrate” (T7 RNAP) is consumed or converted into products. The free DNA-RNAP complex turns on the transcription followed by the translation of GFP (Figure 12A). The dynamics of mRNA are determined by production and degradation, with rate constants of k_{TX} (1/s) and d (1/s), respectively. Ribosomes then bind to the ribosome binding site (RBS) of the mRNA and turn on the translation of GFP_dark with a rate constant of k_{TL} (1/s). GFP_dark undergoes folding and maturation with a rate constant of k_{mat} (1/s), resulting in fluorescent GFP (Figure 12A). In this study, we focused only on the initial TXTL reactions in the first ~4000 s, wherein the reactions reach their maximal production rates (steady states) and are not limited by the available amino acids, energy sources, and/or other components. Since TetR forms stable homodimers (Krafft et al., 1998), TetR in this model represents its homodimer. With these simplifications and assumptions,

we thus have the reaction scheme for TXTL regulated by TetR in the cell-free system (Figure 12A).

Based on the binding and reaction scheme (Figure 12A), we used the general binding block (Figure 8A) and designed a circuit (Figure 12B) that exactly describes the kinetics of the binding interactions and reactions for the regulated TXTL in the cell-free system. In this circuit (Figure 12B), the binding block (blue box) has voltage inputs of initial $[DNA_0]$ for total plasmid concentration, $[RNAP_0]$ for total T7 RNAP concentration, and $[TetR_0]$ for total TetR concentration, via the pins of E, S, and I, respectively; free $[TetR]$ and $[RNAP]$ bind to DNA noncompetitively, exactly described by the same circuit as Figures 7D, 8A; among the three outputs, only the $[DNA-RNAP]$ turns on the transcription; the mRNA is then bound by ribosomes, which results in GFP production. Since several RNAP molecules can bind to one DNA molecule during transcriptional elongation, the average number of T7-RNAP bound in each DNA-RNAP complex would be $1 + k_{TX} * Lm / Cm$ where 1 is the one RNAP binding to the promoter, k_{TX} is the transcription rate (1/s), Lm is the length of mRNA (nt), and Cm is the average RNAP velocity during elongation (nt/s) (Bremer et al., 2003; Marshall and Noireaux, 2019). Therefore, for each DNA-RNAP complex the number of RNAP, $1 + k_{TX} * Lm / Cm$, has to be subtracted from the total $[RNAP_0]$ pool. Similar to the counting of RNAP copy numbers on each DNA-RNAP complex, for each Ribo-mRNA complex, there are $1 + k_{TL} * Lp / Cp$ ribosomes, where 1 is the one ribosome binding to the ribosome binding site, k_{TL} is the translation rate (1/s), Lp is the GFP coding length of mRNA (nt), and Cp is the ribosome velocity during elongation (nt/s). The last part of the circuit is the GFP production where GFP_{dark} is produced with a rate constant of k_{TL} and consumed to make fluorescent GFP with a rate constant of k_{mat} .

All the kinetic parameters (Supplementary Table S2) used in this model were obtained either from previous studies (Újvári and Martin, 1996; Kamionka et al., 2004; Skinner et al., 2004; Marshall and Noireaux, 2019) under similar conditions or from fitting to our experimental data. The simulation curves fitted our experimental data closely as shown in Figures 12C,D. As expected, as more plasmid was added to the cell-free system more GFP was produced until saturation was reached (up to ~12 nM DNA in our experiments) (Figure 12C), where adding more plasmid would not increase GFP production. In another experiment, when varying amounts of TetR were added to the cell-free system with a constant DNA concentration, GFP production was increasingly repressed by more TetR addition.

3 Discussion

We have shown that the ordinary differential equations used to describe the dynamics of voltages and currents in relatively simple electronic circuits are exactly the same as the ODEs

describing molecular kinetics in chemical reactions and biological systems. Voltages faithfully represent molecular concentrations while currents faithfully represent reaction fluxes. Furthermore, we have built Michaelis-Menten circuits and validated them by using well-defined parameters and by fitting experimental data from enzymatic reactions. Based on the MM circuits, we then developed circuit models for more complicated reactions including various enzyme inhibition types, product feedback inhibition, reversible reactions, two-substrate reactions, and regulated TXTL in a cell-free system. These circuits provide foundational building blocks for kinetic modeling of complex chemical and biological networks in the fields of synthetic biology (such as different types of oscillators), metabolism, and cellular signaling.

Taking advantage of circuit models, we are able to translate reaction schematics directly into circuits and to directly perform rapid kinetic modeling for biochemical reactions/networks without the need for deriving math equations or writing code. Using electronic circuits as a new modeling language can thus enable faster and easier modeling of molecular kinetics than using ODEs and numerical solvers. Importantly, circuit modeling is also very effective for scientific communication. Circuit modeling is not only accurate but also very concise because all the underlying equations and parameters/terms describing molecular kinetics, and the detailed interconnectivity between species/components are visualized and clearly labeled in one circuit.

It is worth noting that our circuit models are made of active transconductor-resistor-capacitor circuits that are more general than the passive-only resistor-based circuits used previously in biogeochemical modeling (Domingo-Félez and Smets, 2020; Tang et al., 2021). Our circuits can simulate steady-state and nonlinear dynamic evolution including loading and non-modularity between arbitrary interacting reactions, stochastics at low molecular copy number, and directly map physical parameters in the molecular domain (e.g., concentrations and rates) to equivalent physical circuit parameters (e.g., voltages and currents) (Sarpeshkar, 2010; Teo and Sarpeshkar, 2020). Thus, our circuits are designed mechanistically even at the molecular level and are flexible for use in a variety of applications. For example, circuit modeling allows us to simulate fundamental biochemical mechanisms such as different types of molecular binding and inhibition between enzyme and substrate/inhibitor/activator (Figures 8, 9). Such models otherwise are challenging to obtain without using many assumptions and mathematical derivations.

It should also be noted that our circuit models are more general and accurate than classic MM kinetics because we don't need the free ligand assumption where $[S_0]$ is assumed to be much greater than $[E_0]$. Instead, subtraction of $[ES]$ and $[P]$ from $[S_0]$ in all of our circuits always ensures exact mass conservation. Similarly, if present, automatic subtraction of $[EI]$ and $[ESI]$ ensures exact mass conservation. These subtractions may not

necessarily improve the model accuracy for normal enzymatic reactions that are run under conditions of $[S_0] \gg [E_0]$ and/or $[I_0] \gg [E_0]$. However, under some circumstances where the concentrations of substrate and/or inhibitor are close to the enzyme concentration, such as the case of our TXTL modeling in the cell-free system (Figure 12), the concentrations of complexes including [ES], [EI] and/or [ESI] account for considerable portions of the total concentrations of $[S_0]$, $[I_0]$ and/or $[E_0]$. Thus, with built-in accounting for the concentrations of these complexes, we can apply circuits more accurately and conveniently than MM equations that may not be accurate under all conditions.

Our circuit modeling approach is unique because it allows for a biological system to be both intuitively visualized and quantitatively simulated within a single interactive and graphical software program (e.g., Cadence, CircuitLab). Professional circuit-design software directly enables model-order reduction, hierarchy, modular scalable design, and 25 + forms of sophisticated built-in mathematical analysis, including transient, steady state, frequency response, parametric variation, noise, Monte-Carlo, and other analyses automatically (Teo et al., 2019a; Teo and Sarpeshkar, 2020). Sophisticated adaptive Runge-Kutta and other numerical convergence tools are built into the circuit software preventing the user from having to focus on them. Although many useful tools exist for creating models in systems biology, such as SBML (Hucka et al., 2003) and BioCRNpyler (Poole et al., 2022), these tools require coding skills and are not as convenient to use as circuit design tools that fully take advantage of pictorial and architectural design. Therefore, we believe that our circuit approach will be significantly easier to use for experimental biologists. Synthetic biologists, who are typically more mathematically inclined, will also appreciate the quantitative design aspects and great flexibility that directly port from electronic circuit design to biological circuit design.

Our approach leverages the scalability and modularity of electronic circuit design with built-in hierarchy and circuit motifs. Circuit modeling enables modularity without sacrificing accuracy (e.g., due to the built-in use-it-and-lose-it feedback loops that automatically incorporate the 'loading' of one reaction module on another reaction module in our approach), which is also essential in scalable design. Circuit modeling also makes model-order reduction or expansion very easy such that the impact of a simple or complex model of any portion of a system on outputs can be evaluated with a few keystrokes. Circuit models are therefore scalable to the design of vast complex circuit networks. Furthermore, our circuit modeling approach directly maps physical parameters to physical parameters such that it is easily generalizable. Consequently, it is also more accurate and flexible even in extreme cases such as when concentrations of enzyme and substrate are comparable, enabling detailed models of molecular binding and enzymatic inhibition (Figures 8, 9). With such scalability and flexibility, we anticipate our circuit

modeling approach will become a powerful tool to analyze the behaviors of large biological networks and to mine useful natural algorithms in such systems.

Computational time is an important issue for modeling complicated systems. Since our circuit modeling approach uses similar numerical algorithms (built into the circuit design software) as traditional ODE modeling, we do not expect advancement in computational time between the two modeling methods. Circuit software has some overhead in it to enable graphical design and multiple forms of analysis so it typically leads to a slight increase in simulation time, especially for small networks. For example, depending on the complexity and scale of circuits, the simulation takes a few seconds for small circuits (most circuits in this work) and a few minutes or longer for very large circuits. Running an ODE solver in MATLAB gave identical results to those obtained by circuit simulations in Cadence (Supplementary Figure S4). The MATLAB ODE solver was found to be faster than Cadence in that case (several tenths of a second vs. several seconds) due to the overhead being more significant for a small network. For large-scale models, hardware integrated circuits, namely, cytomorphic chips can run simulations of the "virtual" circuit models at speeds orders of magnitude faster than normal computers (Sarpeshkar, 2010; Woo et al., 2015; Woo et al., 2018). Cytomorphic chips integrate many fundamental biochemical reaction motifs, whose parameters and connectivity can be programmed to run simulations of arbitrary chemical networks. On such integrated circuit chips, the voltages (concentrations) and currents (rates) are emulated in a parallel fashion, even for highly stochastic simulations, rather than simulated. They are almost instantaneously accessible in a MATLAB interface that both programs and reads data from the chips. The computation time of the cytomorphic chips is independent of the reaction network's size and complexity even for stochastic simulations, which cannot be parallelized to represent Poisson noise in digital simulations (Kim et al., 2018). For example, models of computation time can be significantly reduced by several orders of magnitude for circuit models including oscillatory repressilators and more complex networks in cancer (Woo et al., 2015; Teo and Sarpeshkar, 2020) or in SARS-COV2 infection (Beahm et al., 2021).

4 Conclusion

Circuit modeling is advantageous for rapid design and accurate kinetic modeling of chemical and biological systems. Circuit models visualize all math equations and their relationships in one circuit, which is very concise and convenient for effective communication. This approach takes advantage of the high scalability in circuit design and has wide applicability. We envision that circuit modeling could be adopted

as a new language for kinetic modeling and promote scientific communication in the fields of biochemistry, systems biology, biogeochemistry, and synthetic biology.

5 Methods and materials

All enzymes and chemicals were purchased from Sigma Aldrich unless otherwise mentioned. Three enzymes used in this study were beta-galactosidase from *E. coli* (cat# G5635), rabbit muscle lactate dehydrogenase (cat# L2500), and yeast alcohol dehydrogenase (cat# A7011).

5.1 Enzymatic assays

All enzymatic assays were run in 96-well plates (Costar, cat#3595) with 100 μ l of reaction mixture per well and reactions were monitored in real time by using a microplate reader (Molecular Devices Inc.).

Beta-galactosidase (beta-Gal) assays were performed using o-nitrophenyl- β -D-galactopyranoside (ONPG) as substrate. All reagents were prepared in PBS buffer (pH7.2) with 5 mM Dithiothreitol (DTT) and 4 mM MgCl₂. The reactions (100 μ l/well) with varying concentrations of ONPG were monitored by measuring the absorbance of the product, 2-nitrophenol, at 420 nm in real time for over 20 min. The concentrations of the product were determined by a calibration curve that was made by using a freshly prepared 2-nitrophenol solution under the same condition. Initial reaction rates were calculated from the slopes of each reaction curve normally within the first 6–8 min. For competitive inhibition, phenylethyl beta-D-thiogalactopyranoside (PETG), a known competitive inhibitor of beta-Gal (Xu and Ewing, 2004), was added to the reactions under the same condition. For the product feedback inhibition, galactose at varying concentrations was added to the reaction mixture before running the enzymatic assay.

The lactate dehydrogenase (LDH) assay was performed in 96-well plates using a constant concentration of 2 mM NAD⁺ and varying the concentration of lactate as substrate. All reagents were prepared in 0.5 M glycine buffer (pH9.5). The end product NADH concentration was determined by measuring absorbance at 350 nm with a calibration curve pre-established under the same condition. All the reactions (100 μ l/well) were monitored in real time in 96-well plates by a microplate reader. For modeling non-competitive inhibition, oxamate was used as a non-competitive inhibitor of LDH, in the lactate oxidation direction (Powers et al., 2007). The alcohol dehydrogenase (ADH) assay was performed in 40 mM Tris buffer (pH8.3) by using a constant concentration of 4 mM NAD⁺ and varying the concentration of ethanol as substrate. The reactions were monitored similarly to the LDH assay.

All experiments were done with three replicates unless otherwise mentioned. Control reactions without any enzyme were also included in each experiment as blanks. The kinetic parameters including K_m , K_i , V_{max} , and k_{cat} , were derived from Lineweaver-Burk plotting. These experimentally obtained kinetic parameters and initial concentrations were put into the corresponding circuit models before running simulations.

5.2 Transcription and translation in the cell-free system

The cell-free *E. coli* protein synthesis system was purchased from New England BioLabs (cat# E5360). The T7 RNA Polymerase (NEB, cat# M0251S) and RNase Inhibitor (NEB, cat#M0314S) were added to the reaction mixture. The transcription and translation reactions (15 μ l/each) with varying concentrations of plasmid DA313 and purified TetR were run in a 384-well plate (ThermoFisher Scientific, cat# 12-566-2). The reactions were monitored in real time by measuring GFP fluorescence at Ex485/Em528 in a microplate reader (Molecular Devices Inc.). The plasmid DA313 was made by fusing fragments of a hybrid T7 promoter with a tetO binding site (Jung et al., 2020), 5'UTR sequence, and a superfolder GFP (sfGFP) gene into the backbone of pJBL7010 (Silverman et al., 2019) by Gibson assembly (NEB, cat# E2621L). The 5'UTR sequence includes an mRNA stability hairpin (Carrier and Keasling, 1999; Silverman et al., 2019) and a ribosome binding site that was designed by the RBS calculator (Salis, 2011). The plasmid DA313 was purified by Monarch plasmid miniprep kit (New England BioLabs, cat# T1010S) and its concentration was determined by a fluorometric assay with a DNA-specific dye EvaGreen (Ihrig et al., 2006). The sfGFP concentration was estimated by a pre-established calibration curve using a pure EGFP (BioVision, cat#4999-100) with a conversion factor of 1.6 to account for different fluorescent brightness between sfGFP and EGFP (Fluorescent Protein Database, <https://www.fpbse.org/>). All experiments were performed with three independent replicates.

The recombinant TetR with 6xHis tag was over-expressed in *E. coli* JM109 (DE3) with plasmid DA303 and purified using Nickel-NTA agarose resin (ThermoFisher Scientific, cat# 88221). The purity of the recombinant TetR was analyzed by SDS-PAGE gel and the concentration was measured by BCA assay (ThermoFisher Scientific, cat#23252). Since TetR forms stable homodimers (Krafft et al., 1998) its concentration is then converted to the molar concentration of the homodimer. The plasmid DA303 was made by fusing TetR into the pQE80 backbone by Gibson assembly. All plasmids used were confirmed by Sanger sequencing and their maps are provided in the supplemental material (Supplementary Figure S5).

5.3 Circuit design and simulation

All circuits were designed and simulated in sophisticated circuit software including Cadence Virtuoso (version IC6.1.6–64b.500.6, Cadence Design Systems, Inc.) and an online tool, CircuitLab (<https://www.circuitlab.com/>). To design circuits, electric components such as capacitors, resistors, grounds, voltage sources, current sources/generators, and math functions (adders, subtractors, multipliers) were chosen directly from the library in the software and placed into the design window. All components were then wired together to make a circuit according to the system being modeled. Parameters and initial conditions were assigned to each component before running the simulations in the software. As examples, three circuits designed in this work are provided on the CircuitLab website via the links below:

Enzyme inhibitions: (<https://www.circuitlab.com/circuit/5jsn32mbt42d/enzyme-inhibition/>); Two-substrate enzymatic reactions: (<https://www.circuitlab.com/circuit/fk2rya5d6s2p/eab-reaction/>); Cell-free system: (<https://www.circuitlab.com/circuit/5n6sug25t29j/cell-free-simulation/>).

Parameters may need changes to fit the specific condition of the simulation. Other circuits were designed and simulated in Cadence. The design files (schematics) and simulation settings (cellview simulation states) for the Cadence circuits are included in the [Supplementary Material](#). For comparison of ODE coding and circuit modeling, the MATLAB (R2020a, Mathworks) ODE solution code used to simulate the reversible reaction is also included in the [Supplementary Material](#).

Data availability statement

All supporting data generated or analyzed in this study are included in this published article and the [Supplementary Material](#) or are available upon request to the corresponding author.

References

- Alves, R., Antunes, F., and Salvador, A. (2006). Tools for kinetic modeling of biochemical networks. *Nat. Biotechnol.* 24, 667–672. doi:10.1038/nbt0606-667
- Beahm, D. R., Deng, Y., Riley, T. G., and Sarpeshkar, R. (2021). Cytomorphic electronic systems: A review and perspective. *IEEE Nanotechnol. Mag.* 15, 41–53. doi:10.1109/MNANO.2021.3113192
- Bevc, S., Konc, J., Stojan, J., Hodošček, M., Penca, M., Praprotnik, M., et al. (2011). Enzo: A web tool for derivation and evaluation of kinetic models of enzyme catalyzed reactions. *PLoS One* 6, e22265. doi:10.1371/journal.pone.0022265
- Bremer, H., Dennis, P., and Ehrenberg, M. (2003). Free RNA polymerase and modeling global transcription in *Escherichia coli*. *Biochimie* 85, 597–609. doi:10.1016/S0300-9084(03)00105-6

Author contributions

YD, DB, and RS conceived and designed the circuits and projects; YD and XR conducted the experiments and collected all the data; YD and DB analyzed the data, and performed circuit modeling and simulation; YD and TR made the circuit schematics; YD wrote the manuscript and all authors revised and approved the final manuscript.

Funding

This work was supported by AFOSR under grant number FA9550-18-1-0467 and by the NIH under grant number R01 GM 123032-01 to R. Sarpeshkar.

Conflict of interest

The authors declare that the research was conducted in the absence of any commercial or financial relationships that could be construed as a potential conflict of interest.

Publisher's note

All claims expressed in this article are solely those of the authors and do not necessarily represent those of their affiliated organizations, or those of the publisher, the editors and the reviewers. Any product that may be evaluated in this article, or claim that may be made by its manufacturer, is not guaranteed or endorsed by the publisher.

Supplementary material

The Supplementary Material for this article can be found online at: <https://www.frontiersin.org/articles/10.3389/fbioe.2022.947508/full#supplementary-material>

- Carrier, T. A., and Keasling, J. D. (1999). Library of synthetic 5' secondary structures to manipulate mRNA stability in *Escherichia coli*. *Biotechnol. Prog.* 15, 58–64. doi:10.1021/bp9801143

- Daniel, R., Rubens, J. R., Sarpeshkar, R., and Lu, T. K. (2013). Synthetic analog computation in living cells. *Nature* 497, 619–623. doi:10.1038/nature12148

- Deng, Y., Beahm, D. R., Ionov, S., and Sarpeshkar, R. (2021). Measuring and modeling energy and power consumption in living microbial cells with a synthetic ATP reporter. *BMC Biol.* 19, 101–121. doi:10.1186/s12915-021-01023-2

- Dickinson, F. M., and Dickenson, C. J. (1978). Estimation of rate dissociation constants involving ternary complexes in reactions catalysed by yeast alcohol dehydrogenase. *Biochem. J.* 171, 629–637. doi:10.1042/bj1710629

- Domingo-Félez, C., and Smets, B. F. (2020). Modeling denitrification as an electric circuit accurately captures electron competition between individual reductive steps: The activated sludge model-electron competition model. *Environ. Sci. Technol.* 54, 7330–7338. doi:10.1021/acs.est.0c01095
- Eshtewy, N. A., and Scholz, L. (2020). Model reduction for kinetic models of biological systems. *Symmetry (Basel)* 12, 863–922. doi:10.3390/SYM12050863
- Ganzhorn, A. J., Green, D. W., Hershey, A. D., Gould, R. M., and Plapp, B. V. (1987). Kinetic characterization of yeast alcohol dehydrogenases. Amino acid residue 294 and substrate specificity. *J. Biol. Chem.* 262, 3754–3761. doi:10.1016/s0021-9258(18)61419-x
- Hucka, M., Finney, A., Sauro, H. M., Bolouri, H., Doyle, J. C., Kitano, H., et al. (2003). The systems biology markup language (SBML): A medium for representation and exchange of biochemical network models. *Bioinformatics* 19, 524–531. doi:10.1093/bioinformatics/btg015
- Ihrig, J., Lill, R., and Mühlenhoff, U. (2006). Application of the DNA-specific dye EvaGreen for the routine quantification of DNA in microplates. *Anal. Biochem.* 359, 265–267. doi:10.1016/j.ab.2006.07.043
- Jung, J. K., Alam, K. K., Verosloff, M. S., Capdevila, D. A., Desmau, M., Clauer, P. R., et al. (2020). Cell-free biosensors for rapid detection of water contaminants. *Nat. Biotechnol.* 38, 1451–1459. doi:10.1038/s41587-020-0571-7
- Kamionka, A., Bogdanska-Urbaniak, J., Scholz, O., and Hillen, W. (2004). Two mutations in the tetracycline repressor change the inducer anhydrotetracycline to a corepressor. *Nucleic Acids Res.* 32, 842–847. doi:10.1093/nar/gkh200
- Kim, J., Woo, S. S., and Sarpeshkar, R. (2018). Fast and precise emulation of stochastic biochemical reaction networks with amplified thermal noise in silicon chips. *IEEE Trans. Biomed. Circuits Syst.* 12, 379–389. doi:10.1109/TBCAS.2017.2786306
- Krafft, C., Hinrichs, W., Orth, P., Saenger, W., and Welfle, H. (1998). Interaction of Tet repressor with operator DNA and with tetracycline studied by infrared and Raman spectroscopy. *Biophys. J.* 74, 63–71. doi:10.1016/S0006-3495(98)77767-7
- Marshall, R., and Noireaux, V. (2019). Quantitative modeling of transcription and translation of an all-E. coli cell-free system. *Sci. Rep.* 9, 11980. doi:10.1038/s41598-019-48468-8
- Néant, N., Lingas, G., Le Hingrat, Q., Ghosn, J., Engelmann, I., Lepiller, Q., et al. (2021). Modeling SARS-CoV-2 viral kinetics and association with mortality in hospitalized patients from the French COVID cohort. *Proc. Natl. Acad. Sci. U. S. A.* 118, e2017962118. doi:10.1073/pnas.2017962118
- Nguyen, T.-H., Splechtina, B., Steinböck, M., Kneifel, W., Lettner, H. P., Kulbe, K. D., et al. (2006). Purification and characterization of two novel beta-galactosidases from *Lactobacillus reuteri*. *J. Agric. Food Chem.* 54, 4989–4998. doi:10.1021/jf053126u
- Plapp, B. V. (2010). Conformational changes and catalysis by alcohol dehydrogenase. *Arch. Biochem. Biophys.* 493, 3–12. doi:10.1016/j.abb.2009.07.001
- Poole, W., Pandey, A., Shur, A., Tuza, Z. A., and Murray, R. M. (2022). BioCRNpyler: Compiling chemical reaction networks from biomolecular parts in diverse contexts. *PLoS Comput. Biol.* 18, e1009987–19. doi:10.1371/journal.pcbi.1009987
- Portaccio, M., Stellato, S., Rossi, S., Bencivenga, U., Mohy Eldin, M. S., Gaeta, F. S., et al. (1998). Galactose competitive inhibition of β -galactosidase (*Aspergillus oryzae*) immobilized on chitosan and nylon supports. *Enzyme Microb. Technol.* 23, 101–106. doi:10.1016/S0141-0229(98)00018-0
- Powers, J. L., Kiesman, N. E., Tran, C. M., Brown, J. H., and Bevilacqua, V. L. H. (2007). Lactate dehydrogenase kinetics and inhibition using a microplate reader. *Biochem. Mol. Biol. Educ.* 35, 287–292. doi:10.1002/bmb.74
- Resat, H., Petzold, L., and Pettigrew, M. F. (2009). “Kinetic modeling of biological systems,” in *Computational systems biology*, eds. R. Iretton, K. Montgomery, R. Bumgarner, R. Samudrala, and J. McDermott (Totowa, NJ: Humana Press), 311–335. doi:10.1007/978-1-59745-243-4_14
- Salis, H. M. (2011). The ribosome binding site calculator. *Methods Enzymol.* 498, 19–42. doi:10.1016/B978-0-12-385120-8.00002-4
- Sarpeshkar, R. (2010). *Ultra low power bioelectronics: Fundamentals, biomedical applications, and bio-inspired systems*. Cambridge: Cambridge University Press. doi:10.1017/CBO9780511841446
- Silverman, A. D., Kelley-Loughnane, N., Lucks, J. B., and Jewett, M. C. (2019). Deconstructing cell-free extract preparation for *in vitro* activation of transcriptional genetic circuitry. *ACS Synth. Biol.* 8, 403–414. doi:10.1021/acssynbio.8b00430
- Skinner, G. M., Baumann, C. G., Quinn, D. M., Molloy, J. E., and Hoggett, J. G. (2004). Promoter binding, initiation, and elongation by bacteriophage T7 RNA polymerase: A single-molecule view of the transcription cycle. *J. Biol. Chem.* 279, 3239–3244. doi:10.1074/jbc.M310471200
- Tang, J., Riley, W. J., Marschmann, G. L., and Brodie, E. L. (2021). Conceptualizing biogeochemical reactions with an Ohm’s law analogy. *J. Adv. Model. Earth Syst.* 13. doi:10.1029/2021MS002469
- Teo, J. J. Y., Kim, J., Woo, S. S., and Sarpeshkar, R. (2019a). “Bio-molecular circuit design with electronic circuit software and cytomorphic chips,” in 2019 IEEE Biomedical Circuits and systems conference (BioCAS) (IEEE), 1–4. doi:10.1109/BIOCAS.2019.8918684
- Teo, J. J. Y., and Sarpeshkar, R. (2020). The merging of biological and electronic circuits. *iScience* 23, 101688. doi:10.1016/j.isci.2020.101688
- Teo, J. J. Y., Weiss, R., and Sarpeshkar, R. (2019b). An artificial tissue homeostasis circuit designed via analog circuit techniques. *IEEE Trans. Biomed. Circuits Syst.* 13, 540–553. doi:10.1109/TBCAS.2019.2907074
- Teo, J. J. Y., Woo, S. S., and Sarpeshkar, R. (2015). Synthetic biology: A unifying view and review using analog circuits. *IEEE Trans. Biomed. Circuits Syst.* 9, 453–474. doi:10.1109/TBCAS.2015.2461446
- Üjvári, A., and Martin, C. T. (1996). Thermodynamic and kinetic measurements of promoter binding by T7 RNA polymerase. *Biochemistry* 35, 14574–14582. doi:10.1021/bi961165g
- Woo, S. S., Kim, J., and Sarpeshkar, R. (2015). A cytomorphic chip for quantitative modeling of fundamental bio-molecular circuits. *IEEE Trans. Biomed. Circuits Syst.* 9, 527–542. doi:10.1109/TBCAS.2015.2446431
- Woo, S. S., Kim, J., and Sarpeshkar, R. (2018). A digitally programmable cytomorphic chip for simulation of arbitrary biochemical reaction networks. *IEEE Trans. Biomed. Circuits Syst.* 12, 360–378. doi:10.1109/TBCAS.2017.2781253
- Xu, H., and Ewing, A. G. (2004). A rapid enzyme assay for β -galactosidase using optically gated sample introduction on a microfabricated chip. *Anal. Bioanal. Chem.* 378, 1710–1715. doi:10.1007/s00216-003-2317-z
- Zeng, J., Teo, J., Banerjee, A., Chapman, T. W., Kim, J., and Sarpeshkar, R. (2018). A synthetic microbial operational amplifier. *ACS Synth. Biol.* 7, 2007–2013. doi:10.1021/acssynbio.8b00138